Coastal Engineering 194 (2024) 104614

Contents lists available at ScienceDirect

Coastal Engineering

journal homepage: www.elsevier.com/locate/coastaleng

Experimental and numerical investigation of a land-fixed breakwater-type wave energy converter: An OWC device and a porous plate

Qianze Zhuang, Dezhi Ning *, Robert Mayon, Yu Zhou

State Key Laboratory of Coastal and Offshore Engineering, Dalian University of Technology, Dalian 116024, China

ARTICLE INFO

Keywords:
Wave energy converter
Oscillating water column
Experimental and numerical investigation
Porous plate
Land-fixed breakwater

ABSTRACT

To further promote the commercialization of oscillating water column (OWC) devices and expand their application to coastal protection, it is crucial to enhance their survivability as much as possible while improving the wave energy conversion efficiency. In the present study, the hydrodynamic performance of a land-fixed, breakwater-type wave energy converter combining an OWC device and a porous plate was investigated. A series of physical experiments and numerical simulations were conducted to systematically verify each other and select the proper porosity of the porous plate and the gap spacing. On this basis, the effects of wave nonlinearity on hydrodynamic efficiency and wave-induced forces were comprehensively evaluated. The results indicate that under high frequency wave conditions, the porous plate can significantly reduce horizontal forces on the front wall with limited efficiency reduction. This phenomenon is more pronounced under the strong wave nonlinearity. The maximum reduction in horizontal force can reach 52%. At low wave frequencies, the effect of the porous plate is limited as the horizontal forces on the front wall are similar to those without the porous plate. The energy conversion efficiency increases in low frequency wave conditions because the porous plate assists first-order wave energy to enter the chamber by reducing the transfer of wave energy to high-order waves. In addition, due to the dissipation of wave energy by the porous plate, the wave reflection coefficient decreases and the wave dissipation coefficient increases in all cases.

1. Introduction

In recent decades, faced with the growing demand for electricity, renewable energy resources have become a key point in energy development for countries around the world (López et al., 2013; Adcock et al., 2021; Zeng et al., 2024). Among various forms of renewable energy, ocean energy, with abundant reserves has great potential for development, especially wave energy which is characterized by having high energy density (Kamranzad et al., 2022). Research had shown that wave energy can meet more than half of the electricity demands of 44 coastal countries (Shao et al., 2022). However, the utilization of wave energy has not yet entered the commercial operation stage due to the demanding survival challenges associated with the ocean environment (Tiron et al., 2015).

A large number of new wave energy devices are proposed every year. In general, they can be classified into three types of structures based on their working principles, namely the oscillating float type, the oscillating water column (OWC) type, and the overtopping type (López et al., 2013). Among them, the OWC device is currently one of the most reliable and promising wave energy devices, as it has a simple structural form and strong survivability in the ocean environment (Liu et al., 2024). OWC devices can be combined with coastal and offshore structures such as breakwaters and wind turbines to share construction costs. In addition to power generation, the OWC device itself, can serve as a breakwater to dissipate the wave energy near the shore (Simonetti and Cappietti, 2021). Studies on OWC technology mainly focuses on two aspects: improving the energy conversion efficiency of the device, and reducing damage to the device. By combining both research directions, the overall cost-effectiveness of the OWC device can be improved, further promoting its commercialization.

In terms of improving efficiency, Mayon et al. (2023, 2021) have demonstrated through experimental investigation and numerical simulations that coupling an OWC wave energy converter with a parabolic breakwater can significantly increase the upper efficiency limit based the principle of parabolic reflector focusing. Elhanafi et al. (2018) compared the performance of single chamber and dual chamber OWC devices under various testing parameters and concluded that the dual chamber structure can increase the capture width ratio of the device, thus improving its overall energy conversion efficiency in random sea conditions. Furthermore, Fu et al. (2023) conducted numerical research on an OWC system with additional chambers and found that compared

* Corresponding author.
E-mail address: dzning@dlut.edu.cn (D. Ning).

https://doi.org/10.1016/j.coastaleng.2024.104614
Received 10 May 2024; Received in revised form 6 August 2024; Accepted 4 September 2024
Available online 6 September 2024

with the dual chamber system, the five chamber system exhibited higher efficiency under low frequency waves. The above studies were all conducted on a single OWC device, but in practical applications, it is inevitable that multiple OWC devices will be deployed in an array formation. Wang et al. (2023a) analyzed the influence of different coastal scenarios on the wave energy extraction efficiency of an OWC array. The results showed that embedding the array into a straight coast yielded the optimal results. Li et al. (2022c) investigated the performance of a dual chamber OWC array based on potential flow theory and found that compared with the single chamber OWC array, the former had a broader capture bandwidth under both normal and oblique wave conditions. There are many other factors that can affect the energy conversion efficiency of OWC devices. Kamath et al. (2015) used numerical techniques to show that as the incident wavelength increases, the power take off (PTO) damping in the OWC device must increase correspondingly to achieve the maximum energy conversion efficiency of the device. Rezanejad et al. (2019) combined numerical and experimental investigations to demonstrate that certain specific stepped terrains contribute to improving the efficiency of the OWC system. The vast majority of methods mentioned above to improve the energy conversion efficiency of the device will be accompanied by an increase in wave height near the device. This increases the wave loading which is not conducive to the survival of the device.

At present, research on improving the energy conversion efficiency of OWC devices has been relatively comprehensive, but there are still many shortcomings in understanding the physical processes of load application on the devices. In fact, reducing the wave force acting on the device is often more important than improving its efficiency. One of the most renowned OWC prototypes, the Mutriku Wave Power Plant suffered severe structural damage during the construction phase due to wave impacts in stormy weather. The front wall sustained heavy damage, which resulted in a three-year delay in its official completion (Medina-Lopez et al., 2015; Pawitan, 2019). Medina-Lopez et al. (2015) pointed out that when waves impact directly against the OWC structure, cavitation may occur at sharp edges of the front wall, greatly increasing the possibility of structural damage to this component. Martin et al. (2023) studied the characteristics of random wave loads on the external walls of an OWC device using physical experiments and numerical models. The nonlinear wave loads on an array composed of four OWC devices were analyzed, and the results showed that the spacing in the array had a significant impact on the wave forces (Zhou et al., 2022). Wang et al. (2020) investigated the distribution pattern of wave forces and bending moments on a land-based dual-chamber OWC device and proposed a method to reduce the peak wave loads. Ning et al. (2023) found that when the wave height of solitary waves exceeds a certain threshold, overflow occurs at the air orifice of the OWC device, and the wave force acting on the structure will be different from the results predicted by a two-dimensional numerical model.

The use of a porous structure may be a good approach to reduce the wave forces acting on an OWC device. Some structures such as porous plates or porous membranes are common in coastal engineering practice, and often play a role in dissipating wave energy, thereby reducing the load on engineering equipment. Previous researchers have conducted extensive research in this area. Li et al. (2022b) established a semi-analytical model of the interaction between waves and a vertical cylinder with an immersed porous plate using linear potential flow theory. When the wave frequency exceeded a certain critical frequency threshold, the wave load on the cylinder would decrease significantly. Similarly, Ning et al. (2017) theoretically investigated the wave forces acting on truncated cylinders with porous sidewalls in the upper region, and the results showed that the hydrodynamic load was reduced compared with impermeable structures. Poguluri et al. (2022) studied the interaction between multi-layer porous plates and waves and found that in most cases, a double plate structure can achieve higher energy dissipation and smaller wave transmittance. Gayathri et al. (2022), Zheng et al. (2020) analyzed the influence of a flexible porous membrane and porous elastic disks on wave propagation, respectively. The results demonstrated that there is a proper porosity to maximize the wave power dissipation. The above studies have all been completed using an analytical approach. There have also been some experimental and numerical studies. Feichtner et al. (2021b) and Qiao et al. (2021) conducted numerical simulations and experiments on the interaction between waves and fixed porous plates and porous cylinders, respectively. In both studies, porous structures exhibit beneficial effects in wave attenuation and load reduction. Both investigations used the macroscopic porous media method to effectively replace the actual porous structures. This is an advantageous simulation technique that can significantly reduce computational complexity while maintaining accuracy when the flow inside the porous structures is not a concern (Wang et al., 2022a,b, 2023c).

The porous structure mainly dissipates the energy of high-frequency waves, while the energy absorbed by the OWC device is mainly derived from relatively long waves at low frequencies. Then, coupling a porous structure with an OWC device may achieve a significant reduction in the high frequency wave load on the OWC device. At the same time, the energy conversion efficiency of the OWC device can be relatively unaffected. The present research on this topic is very limited. Zhang et al. (2021) studied the hydrodynamic performance of a wave attenuation system integrated with a land-fixed OWC device and a porous plate based on linear potential flow theory. The reflected waves were significantly reduced and the frequency bandwidth of the effective wave attenuation was also increased. Mayon et al. (2022) analyzed the efficiency and wave force by placing multiple layers of small spheres on the seaward wall of an OWC device and obtained positive results. Tsai et al. (2018) conducted numerical and experimental research on an OWC device with a porous wall connected to the seaward wall. Through this modification, the efficiency of the device was improved, while the wave force was also reduced. To the best of the authors' knowledge, the aforementioned examples are the only three relevant studies on combining a porous structure with an OWC. However, some of these studies only considered linear factors and ignored fluid viscosity, others lacked detailed analysis and support from experimental data. This study comprehensively employs high-fidelity numerical simulation techniques and systematic physical model experiments to investigate the hydrodynamic performance of a land-fixed breakwater-type wave energy converter that integrates an OWC device with a porous plate. The focus of the present research is wave-induced forces, wave energy conversion, wave reflection and dissipation under the influence of wave nonlinearity, porosity of the porous plate, and its spacing from the OWC device. The purpose of this study is to provide a possible solution for enhancing the survivability of OWC devices in the ocean environment, and mitigate structural damage similar to that which occurred at the Mutriku Wave Power Plant.

The remainder of this paper is organized as follows. Section 2 presents the experimental set-up, the numerical model and the data analysis method. In Section 3, we first describe the convergence analysis of the numerical model and the validation of the numerical results by comparison with experimental data. Afterwards, appropriate parameters for the porous plate are determined by analyzing the hydrodynamic performance of the OWC device. The remaining part of Section 3 is dedicated to investigating the underlying mechanism of horizontal force application, wave energy conversion, reflection and dissipation under the influence of different wave nonlinearities. Finally, the main conclusions from this study are summarized in Section 4.

2. Methodology

2.1. Experimental setup

The physical model experiments were carried out in a wave–current flume at the State Key Laboratory of Coastal and Offshore Engineering, Dalian University of Technology (DUT). The flume length is 22 m, the

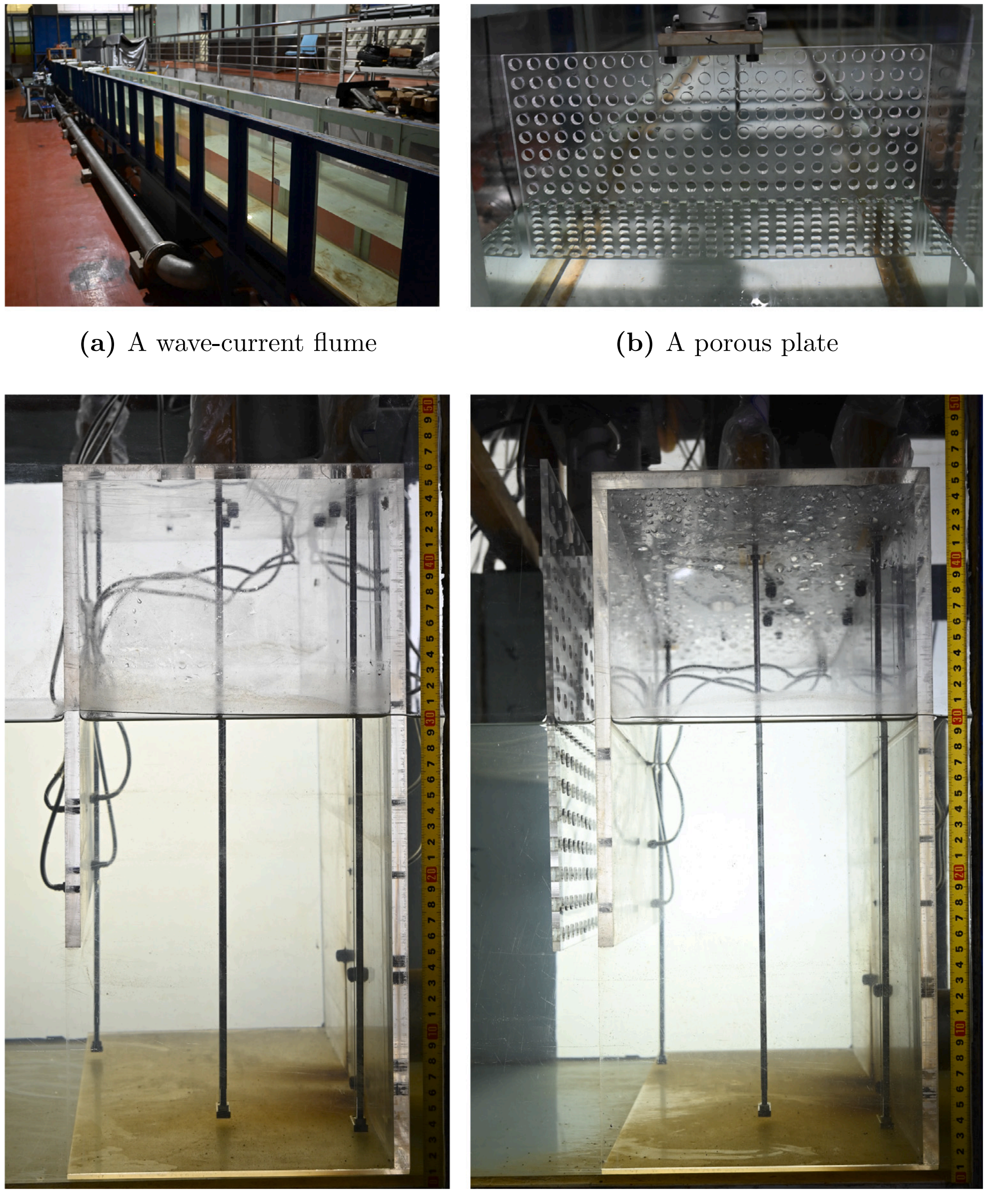

(a) A wave-current flume (b) A porous plate

(c) An OWC model (d) An integrated porous plate-OWC model

Fig. 1. Photographs of (a) the wave–current flume; (b) the porous plate; (c) the land-fixed OWC model and (d) the OWC model integrated with a porous plate.

width is 0.45 m, and the height is 0.6 m. The flume can generate regular and irregular waves with a piston-type wave-making system. There is a sloping beach at one end of the flume to absorb the transmitted waves. A photograph of the flume is shown in Fig. 1(a). Fig. 1(b), (c) and (d) depict three different physical model experiments including the interaction between waves and a porous plate, a land-fixed OWC model, and an integrated system combining the porous plate and the land-fixed OWC model, respectively.

Fig. 2 illustrates the schematic setup of the experiment, which is not drawn to scale for the sake of clarity. Fig. 2(a), (b) and (d) are side views, while Fig. 2(c) is a top view to better illustrate the experimental layout. Taking into account the feasible wave conditions that can be studied in the flume, and the real sea states in coastal waters off China where the significant wave height ranges from 0.5 m to 3.5 m and the wave period from 4 s to 9 s (Li et al., 2022a), the model scale was set to 1:25 in the present study, based on the Froude scaling law. The water depth h in all experiments was 0.3 m.

A series of experiments were first carried out to investigate the interaction between waves and a porous plate. The distances from the porous plate to the stationary position of the wave-maker was 12.77 m. As shown in Fig. 2(a), four wave gauges were arranged in front of the porous plate. The leftmost gauge, G1 was used to confirm the incident wave height. The surface elevations measured by gauges G2–G4 were used to calculate the wave reflection coefficient. This coefficient was calculated using the two-point method (Goda and Suzuki, 1977), which requires that the distance between the closest wave gauge and the structure be not less than 0.25 times the wavelength, and the distance between two wave gauges should be 0.05 times to 0.45 times the wavelength. The spacing between G2, G3 and G4 was fixed at 0.2 m, and the distance from G4 to the porous plate was fixed at 2.8 m, so that the positions of the wave gauges can meet the requirements of the two-point method at all investigated wavelengths. Additionally, two wave gauges G5 and G6 were located behind the porous plate, which were used to measure the height of the transmitted wave. The positions of these two wave gauges also remain fixed for the range of incident wave periods investigated. The porous plate was fixed to a frame above the flume using a load cell F1, and the draft d_p was 0.15 m.

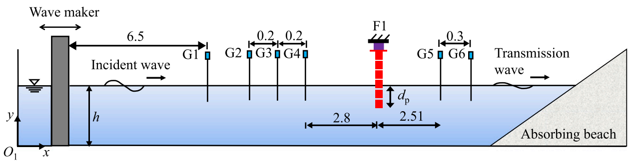

(a) Porous plate experiment (side view)

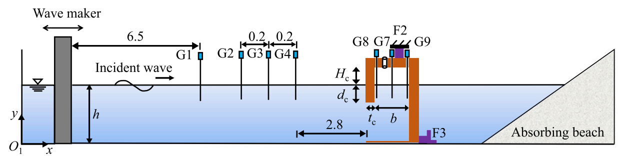

(b) OWC model experiment (side view)

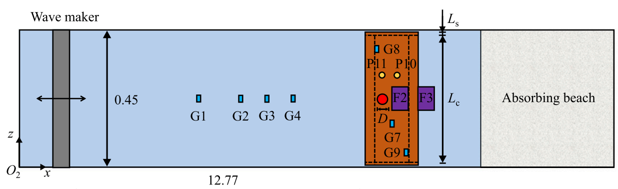

(c) OWC model experiment (top view)

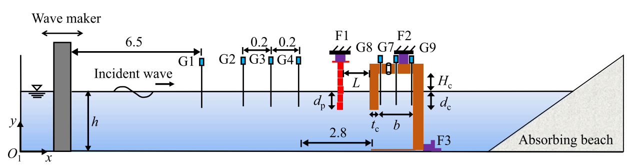

(d) Integrated porous plate-OWC model experiment (side view)

Fig. 2. Schematic diagram of the experimental setup in the wave–current flume: (a) the porous plate experiment viewed from the side; (b) the land-fixed OWC model experiment viewed from the side; (c) the land-fixed OWC model experiment viewed from the top and (d) the integrated porous plate-OWC model experiment viewed from the side (not to scale, unit: m). G1 to G9: wave gauges; P10 and P11: pressure sensors; F1 to F3: load cells.

As shown in Fig. 2(b) and (c), the porous plate was replaced with the land-fixed OWC model. This model was connected to two load cells F2 and F3. F2 was connected to the top surface of the model, while F3 was attached to the back wall, bottom edge of the model. Both were located along the central axis of the flume in the x direction. By adding the x direction component force vectors measured by these load cells, the overall horizontal force on the land-fixed OWC model could be obtained. To ensure the precision of the measured forces, a narrow gap of 0.002 m was provided between the model and the side walls and the bottom of the flume. Three wave gauges G7 to G9 were used to measure the wave elevations inside the chamber. G8 and G9 were positioned 5 mm away from the front and rear walls of the chamber respectively, to obtain the run-up height of the water surface. G7 was located at the center of the chamber and the surface elevation at this position was used to calculate the energy conversion efficiency of the OWC wave energy converter. In small-scale OWC model experiments, the PTO system is often approximated by an air orifice (Wang et al., 2020). In the present study, a circular air orifice was placed on the roof of the OWC model. It was located on the central axis of the flume along the x direction. The distance from its center to the seaward surface of the front wall was 0.08 m. The pressure sensor P11 and the center of the orifice have the same x coordinate, while the x coordinate of

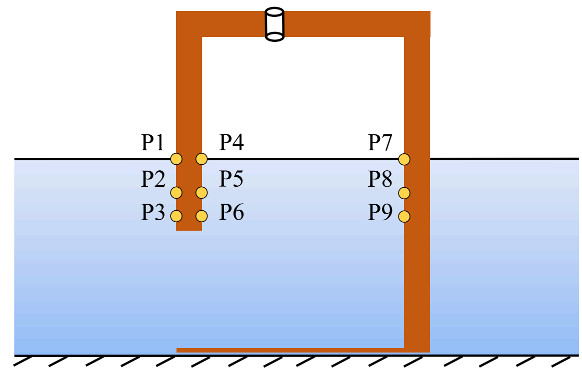

Fig. 3. Distribution of pressure sensors on the front and back walls of the OWC model.

the pressure sensor P10 is 0.06 m further along the flume than that of P11. P10 and P11 both have the same z coordinate, offset 0.1 m from the centerline of the flume. The air pressure obtained by averaging the data from P10 and P11 was used for calculating the energy absorbed by the OWC model. Fig. 3 illustrates the locations of the nine pressure sensors P1 to P9 for measuring the hydrodynamic pressure at the OWC chamber. The sensors were symmetrically distributed on the seaward and shoreward surfaces of the front wall, as well as on the inner side of the back wall. The top layer of sensors were positioned at the static water level. The sensors in the second layer were located at the middle of the front and the back walls. The bottom layer of sensors were 0.055 m lower than the second layer of sensors. Fig. 4 further illustrates the geometry of the OWC model and the arrangement of all measuring instruments on the model. The model was assembled from perspex sheets, which permitted the observation of the wave surface elevation inside the chamber. The front, top and back walls of the model had the same thickness t_c = 10 mm. The thickness L_s of the side walls was 3 mm, which was the same as the thickness of the bottom wall. It should be noted that, for ease of installation, the pressure sensors P1 to P3 and P4 to P6 were symmetrically distributed about the vertical central axis of the seaward surface of the front wall. Since the present study focuses on two-dimensional problems, this arrangement will not affect the accuracy of the measurement data. Photographs of the three types of data acquisition instruments mentioned above are shown in Fig. 5.

Fig. 2(d) shows the OWC model integrated with the porous plate. The two key parameters are the porosity ε of the porous plate and the spacing L between the porous plate and the OWC model. Three levels of porosity ε, ranging from 10%, 20% to 30%, were adopted as shown in Fig. 6. Fig. 7 illustrates the specific dimensions of a typical porous plate, with a width L_p of 0.446 m, a thickness t_p of 0.01 m and a height H_p of 0.32 m. All holes in the porous plate are arranged in a uniform square grid pattern. The spacing between each hole is equal to the side length S of the square grid, which is 0.02 m. The hole diameters vary for different levels of porosity. The porosity ε is defined as the ratio of the void area to the total area of the plate without openings, which can be calculated as:

$$\varepsilon = \frac{\pi r^2}{S^2} \tag{1}$$

where, the radius r was taken as 3.6 mm, 5.1 mm and 6.25 mm, respectively. The following parameters remain constant throughout the experimental investigation: the chamber width $b = 0.2$ m; the chamber front wall draft d_c = 0.15 m; the air chamber height H_c = 0.15 m; the chamber length L_c along the z direction of the flume is equal to 0.44 m. In research on the efficiency of an OWC type wave energy converter, the opening ratio c is one of the significant parameters, which is calculated according to:

$$c = \frac{\pi(\frac{D}{2})^2}{L_c b} \tag{2}$$

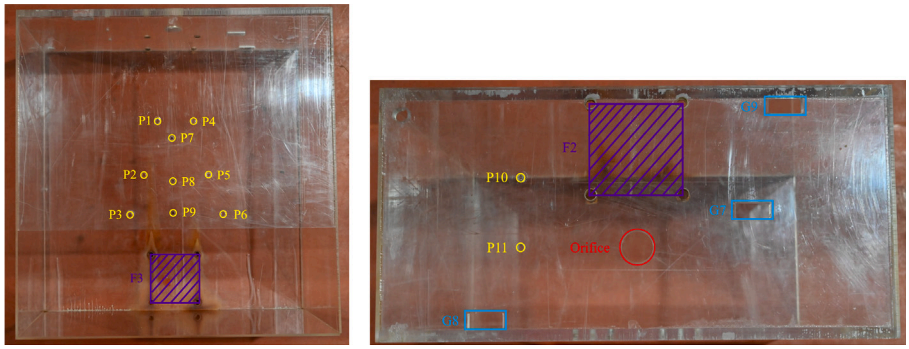

(a) Front view **(b)** Plan view

Fig. 4. Photographs of the OWC model. (a) Front view; (b) Plan view.

(a) A load cell **(b)** A pressure sensor

(c) Wave gauges

Fig. 5. Photographs of the data acquisition instruments. (a) a typical load cell; (b) a typical pressure sensor; (c) wave gauges.

where, D is the orifice diameter. c was selected as 0.66% to achieve the optimal hydrodynamic efficiency in the present study (Ning et al., 2016), with D = 27.2 mm. Three different porous plate separation distances L (0.025 m, 0.05 m and 0.075 m) were investigated, corresponding to one eighth, one fourth and three eighths of the chamber width b, respectively. The ratio of incident wavelength λ to chamber width b ranged from 6 to 13 in the experiments, which is equivalent to a decrease in dimensionless wave frequency kh from 1.57 to 0.72. Furthermore, three different incident wave heights of H_i = 0.03 m, 0.05 m and 0.07 m were considered to analyze the effects of wave nonlinearity. Detailed experimental conditions for three different models are listed in Tables 1–3. Each row includes 13 experimental conditions, representing 13 incident wavelengths.

All data acquisition equipments were carefully calibrated prior to the carrying out of experiments. The sampling frequency of the wave gauges and pressure sensors was 100 Hz, while that of load cells was 200 Hz. Each experimental case was performed at least twice to ensure repeatability, and the final results were the average of the multiple tests taken. It is worth noting that due to the limiting experimental conditions, and the contradiction between Froude similarity and

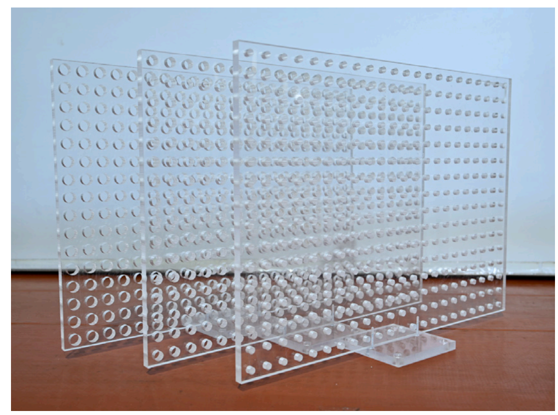

Fig. 6. Three porous plates with different levels of porosity.

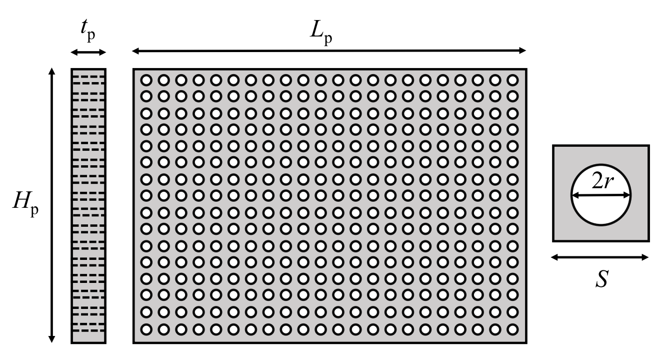

Fig. 7. Schematic of a typical porous plate. Left: side view; Middle: front view; Right: a square grid with a hole in a porous plate.

Table 1
Experimental conditions for the porous plate model.

Case	Wave height H_i (m)	Porosity ε
W_a1-W_a13	0.03	10%
W_a14-W_a26	0.05	10%
W_a27-W_a39	0.07	10%
W_a40-W_a52	0.05	20%
W_a53-W_a65	0.05	30%

Reynolds similarity, the present experiment chose to follow Froude similarity as a preliminary small-scale exploration. It should also be noted that this will result in differences in the air compressibility effects between the model scale and the prototype scale. Air in small models

Table 2
Experimental conditions for the land-fixed OWC model.

Case	Wave height H_i (m)
W_b1-W_b13	0.03
W_b14-W_b26	0.05
W_b27-W_b39	0.07

Table 3
Experimental conditions for the integrated porous plate-OWC model.

Case	Wave height H_i (m)	Porosity ε	Spacing L (m)
W_c1-W_c13	0.03	10%	0.05
W_c14-W_c26	0.05	10%	0.05
W_c27-W_c39	0.07	10%	0.05
W_c40-W_c52	0.05	20%	0.05
W_c53-W_c65	0.05	30%	0.05
W_c66-W_c78	0.05	10%	0.025
W_c79-W_c90	0.05	10%	0.075

can be considered incompressible (Pawitan et al., 2019), while in prototype scale devices, air compressibility can have significant effects on internal air pressure (Viviano et al., 2019). Due to the neglection of air compressibility in this study, the incompressible two phase flow model was used in the subsequent numerical simulations.

2.2. Numerical model

2.2.1. Governing equations

In the present study, two key physical processes are simulated: the gas–liquid coupling process that occurs in the land-fixed OWC for extracting wave energy, and the interaction between the waves and the porous plate. The numerical model uses the standard two-dimensional incompressible Navier–Stokes (NS) equations to simulate air flow and wave motion, omitting the effects of air compressibility in the small-scale air chamber (Simonetti et al., 2018). The Volume-of-Fluid (VOF) technique is used to capture the free surface and simulate the gas–liquid interaction. The governing equations outside the porous plate region are the standard Navier–Stokes equations, whereas in the porous plate region, the momentum equation with an added resistance source term is used as a macroscopic method to simulate the blocking effect of the porous plate. The equations employed are described below. Firstly, the NS equations can be written as:

$$\nabla \cdot \boldsymbol{v} = 0 \tag{3}$$

$$\rho \left(\frac{\partial \boldsymbol{v}}{\partial t} + \boldsymbol{v} \cdot \nabla \boldsymbol{v} \right) = -\nabla P + \rho g + \nu \nabla^2 \boldsymbol{v} \tag{4}$$

where $\boldsymbol{v}$ is the fluid velocity, ρ is the fluid density, t is the physical flow time, P is the fluid pressure, g is the gravitational acceleration, ν is the fluid dynamic viscosity. The parameters $\boldsymbol{v}$, ρ, and ν are calculated using the following formulas in the VOF method (Hirt and Nichols, 1981).

$$\boldsymbol{v} = \alpha \boldsymbol{v}_w + (1-\alpha)\,\boldsymbol{v}_a \tag{5}$$

$$\rho = \alpha \rho_w + (1-\alpha)\,\rho_a \tag{6}$$

$$\nu = \alpha \nu_w + (1-\alpha)\,\nu_a \tag{7}$$

where the subscripts w and a refer to the water and air phases, respectively. α is a content indicator that represents the proportion of water in each grid cell, which can range from 0 to 1. $\alpha = 0$ denotes that only air exists in the cell, $\alpha = 1$ indicates that the cell is filled with water. If $0 < \alpha < 1$, the cell is considered to be in the transition area from air to water. Specifically, when $\alpha = 0.5$, the cell is treated as the contour of the free surface. α should meet with the following transport equation requirements (Rusche, 2003):

$$\frac{\partial \alpha}{\partial t} + \nabla \cdot (\boldsymbol{v}\alpha) + \nabla \cdot \boldsymbol{v}_c \alpha (1-\alpha) = 0 \tag{8}$$

where $\boldsymbol{v}_c$ is the artificial compression velocity used to reduce diffusion effects.

For most engineering problems, the key factor in the interaction between fluids and porous structures is the pressure drop ΔP, which represents the difference in pressure before and after the fluid passes through a porous structure. It can be written as follows (Feichtner et al., 2021b):

$$\Delta P_i = \rho \left(d_i v_i + \frac{f_i}{2} \left| v_i \right| v_i + l_i \frac{\partial v_i}{\partial t} \right) \tag{9}$$

where ΔP_i is the change in fluid pressure in the ith direction. d_i, f_i and l_i are the i components of the linear coefficient, the quadratic coefficient, and the transient coefficient respectively. v_i is the fluid velocity in the ith direction near the porous structure. The first term on the right side of Eq. (9) is linearly related to the fluid velocity, representing the contribution of viscous friction to the pressure drop. Generally, viscous losses do not play a dominant role when water waves interact with thin porous structures (Sollitt and Cross, 1972). Therefore, the linear term can be neglected in the present study. The third term is related to the acceleration of the fluid as it passes through the openings, and Molin (2011) observed that this term tended to zero when the scale of the openings was much smaller than the wavelength. For this research, the second item is the main source of the pressure drop, which represents turbulent drag. In summary, the pressure drop formula can be reduced to:

$$\Delta P_i = \rho \frac{f_i}{2} \left| v_i \right| v_i \tag{10}$$

Molin (2011) provided a formula for calculating the coefficient f_i:

$$f_i = \frac{1 - \varepsilon_i}{\delta \varepsilon_i^2} \tag{11}$$

where ε_i is the porosity of a porous structure in the ith direction. δ is an empirical discharge coefficient ranging from 0.4 to 0.5 (Feichtner et al., 2021b). Based on previous literature (Qiao et al., 2020; Feichtner et al., 2021a; Mackay and Johanning, 2020), the present work takes the value of δ as 0.5. Subsequently, the added resistance source term $\boldsymbol{R}$ in the porous region can be derived as:

$$\boldsymbol{R} = (R_x, R_y) \tag{12}$$

$$R_i = \frac{-\Delta P_i}{n_i} = \frac{-\rho f_i}{2 n_i} \left| v_i \right| v_i \quad \text{for } i = x, y \tag{13}$$

where R_i is the component of $\boldsymbol{R}$ along the i axis and n_i is the thickness of a porous structure in the ith direction. The revised momentum equation for the porous region can then be written as:

$$\rho \left(\frac{\partial \boldsymbol{v}}{\partial t} + \boldsymbol{v} \cdot \nabla \boldsymbol{v} \right) = -\nabla P + \rho g + \nu \nabla^2 \boldsymbol{v} + \boldsymbol{R} \tag{14}$$

2.2.2. Numerical wave flume

Three types of two-dimensional numerical wave flumes were established to reflect the experimental setups presented in Fig. 2. Fig. 8(a) shows a typical wave tank model to simulate the interaction between the waves and the land-fixed OWC. A Cartesian coordinate system O-xy was set at the bottom left corner of the computational domain. The positive x axis was orientated in the direction of the wave propagation and the positive y axis was in the vertically upwards direction. The left side of this wave flume was programmed with the velocity inlet boundary, which was used to generate the required water waves. For second-order stokes wave theory, the water surface elevation η, the horizontal and vertical water particle velocity components u_x and u_y can be calculated from Eqs. (15)–(17), respectively:

$$\eta = \frac{H_i}{2} \cos(kx - \omega t) + \frac{\pi H_i^2}{4\lambda} \left(1 + \frac{3}{2\sinh^2(kh)} \right) \coth(kh) \cos 2(kx - \omega t) \tag{15}$$

$$u_x = \frac{H_i \omega \cosh k(y+h)}{2\sinh(kh)} \cos(kx - \omega t) + \frac{3k\omega H_i^2}{16} \frac{\cosh 2k(y+h)}{\sinh^4(kh)} \cos 2(kx - \omega t) \tag{16}$$

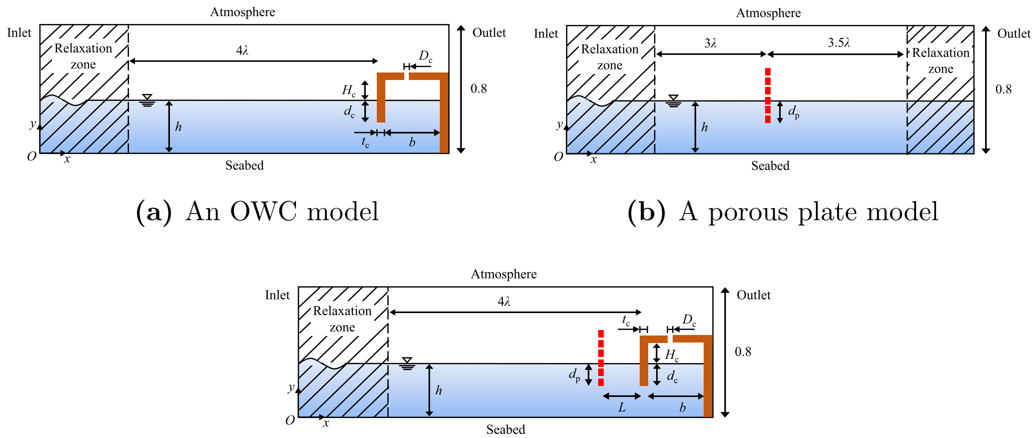

(a) An OWC model
(b) A porous plate model
(c) An integrated porous plate-OWC model

Fig. 8. Schematic of the numerical wave flume and (a) the land-fixed OWC model; (b) the porous plate; (c) the integrated porous plate-OWC model (unit: m).

$$u_y = \frac{H_i \omega \sinh k(y+h)}{2\sinh(kh)} \sin(kx-\omega t) + \frac{3k\omega H_i^2}{16} \frac{\sinh 2k(y+h)}{\sinh^4(kh)} \sin 2(kx-\omega t) \quad (17)$$

where k is the wave number; ω represents the circular frequency of the incident waves; t is the time. This wave theory can only characterize the evolution of second-order components in waves and second-order contributions of wave–structure interaction. It should be noted that current research only considers regular waves. When further considering the nonlinear effects of irregular waves, the above theory needs to be revised. The upper surface of the tank was set as an atmospheric boundary condition. Both the seabed and the surface of the land-fixed OWC had no-slip boundaries applied. The right end boundary of the flume was divided into two parts by the back wall of the OWC, with the upper part being the atmospheric boundary and the lower part being the fixed wall boundary. The front and back sides of the wave tank were set as empty boundaries since it was a two-dimensional model. A relaxation zone was defined at the front section of the flume using the open source toolbox, waves2Foam (Jacobsen et al., 2012). The fluid velocity $\boldsymbol{v}$ in the relaxation zone was corrected by the following formula:

$$\boldsymbol{v} = (1-\tau)\,\boldsymbol{v}_{\mathrm{ref}} + \tau \boldsymbol{v}_{\mathrm{num}} \quad (18)$$

where τ was the weighting factor, $\boldsymbol{v}_{\mathrm{ref}}$ was the fluid velocity calculated based on a predetermined wave theory and $\boldsymbol{v}_{\mathrm{num}}$ was the numerical fluid velocity. τ increased from 0 to 1 as the x coordinate transitioned from the left side to the right side of the relaxation zone (Wang et al., 2023b). In the remaining areas of the wave flume, τ remained constant with unit value. Using the relaxation technique, the secondary reflected waves can be eliminated and the accuracy of the generated waves can be guaranteed. In the current numerical study, the incident wavelength λ and wave height H_i ranged from 1.2 m to 3.6 m, and from 0.03 m to 0.1 m, respectively. Compared with the experimental cases, additional wavelengths of 2.8 m, 3.2 m, 3.6 m, and an additional wave height of 0.1 m was investigated. Based on the wave classification system of Le Méhauté (Le Méhauté, 2013), all cases with weak wave nonlinearity were generated using second-order Stokes wave theory. The fifth-order Stokes wave theory was used for other conditions due to the strong wave nonlinearity. It should be noted that the length of the numerical wave flume changes with the variation of the incident wavelength. The flume was set equal to the length (2λ) of the relaxation zone plus the distance (4λ) from the OWC model to the relaxation zone plus the length (0.21 m) of the OWC model. This method could effectively reduce the number of grid cells in the numerical models. The height and width of the water tank were maintained at 0.8 m and 0.44 m, respectively. The majority of the physical parameters in the numerical wave flume were the same as those in the experiment, except for the shape and absolute size of the orifice in the OWC model. In the two-dimensional numerical model, the orifice was equivalent to a narrow rectangular opening. Its width D_c was calculated as 0.00132 m using Eq. (19) to ensure that the opening ratio c was maintained equal to 0.66%.

$$c = \frac{D_c}{b} \quad (19)$$

In addition, the center of the orifice was kept in the same position as that in the physical model. As shown in Fig. 8(b), there were two relaxation zones in the numerical wave flume when only the porous plate is under consideration. The left end relaxation zone is the same as that in Fig. 8(a), while the right end relaxation zone is set to eliminate transmitted waves, with a length of 1.5λ. The weight factor τ decreases from 1 to 0 along the positive x axis direction in the right relaxation zone. The mesh at a distance of 3λ from the left relaxation zone has multiple levels of refinement. The modified NS equation was applied in this area to simulate the obstructive effect of the porous plate on water wave propagation. By combining the models in Fig. 8(a) and (b), the interaction between waves and the OWC model integrated with the porous plate can be investigated, as shown in Fig. 8(c).

In the present work, all numerical wave flumes were established using *blockMesh*, the native meshing utility of OpenFOAM, to obtain the best mesh quality. The governing equations were discretized by the finite volume method (FVM), and the various equation terms used different numerical schemes. The time derivative term was calculated using the Crank–Nicolson scheme, with a mixing factor of 0.3 (Larsen et al., 2019). The gradient, convection, and Laplacian terms were discretized using the Gaussian linear scheme, the Gauss upwind scheme, and the Gaussian linear correction scheme, respectively. To balance the computational accuracy and speed, this numerical study adopted the self-adapting time step method (Li and Zhang, 2019). The time step Δt at different times varied according to the velocity of the fluid, under the limitation of the Courant number C_o, which can be defined as:

$$C_o = \frac{|\boldsymbol{U}|\,\Delta t}{\Delta m} \quad (20)$$

where $|\boldsymbol{U}|$ was the absolute value of the maximum fluid velocity in the computational domain, Δm was the length of a specific mesh cell in the direction of maximum fluid velocity. The PIMPLE algorithm was used to solve the velocity pressure coupling, which is a combination of the PISO (Pressure-Implicit with Splitting of Operators) algorithm (Issa, 1986) and the SIMPLE (Semi-Implicit Method for Pressure-Linked Equations) algorithm (Van Doormaal and Raithby, 1984).

2.3. Data analysis

A typical land-fixed OWC type wave energy converter has a multi-stage energy conversion efficiency. This study focuses on the first stage, which is the efficiency of converting the wave energy into the kinetic energy of the air flow at the orifice of the OWC device. This efficiency greatly determines the amount of energy that the wave energy converter can ultimately yield. It can be calculated as follows:

$$\xi = \frac{P_a}{P_w w} \tag{21}$$

where ξ is the energy conversion efficiency, P_a is the wave power absorbed by the OWC model, P_w represents the average incident wave energy flux per unit width wave crest and w signifies the width of the waves incident upon the OWC device, which is equal to L_c in the present work. P_w is calculated using the following formulas based on the linear potential flow theory:

$$P_w = \frac{1}{2}\rho g(\frac{H_i}{2})^2 v_g \tag{22}$$

$$v_g = \frac{v_w}{2}(1 + \frac{2kh}{\sinh 2kh}) \tag{23}$$

$$v_w = \frac{\omega}{k} \tag{24}$$

where v_g is the incident wave group velocity, v_w is the incident wave velocity. k and ω satisfy the dispersion equation:

$$\omega^2 = gk\tanh(kh) \tag{25}$$

Based on the assumption of air incompressibility, P_a is obtained from the following formula:

$$P_a = \frac{1}{T}\int_t^{t+T} Q(t)p(t)dt = \frac{bw}{T}\int_t^{t+T} v_c(t)p(t)dt \tag{26}$$

where T is the incident wave period, Q is the air flux through the orifice per unit time, p represents the air pressure inside the chamber and v_c is the velocity of the periodically oscillating water surface in the chamber. In the experimental investigation, the pressure data measured by the pressure sensors P10 and P11 was averaged to obtain p. The first derivative of the wave elevation measured by the wave gauge G7 was calculated to obtain v_c. In theory, the pressure p should reach its peak value when the speed v_c reached its maximum value, however, there was a slight delay in the actual data recording due to the acquisition instruments. Therefore, phase matching between the p and v_c time histories was performed. In addition, the instant when the secondary reflected wave reached the OWC model in the different cases was calculated. P_a was chosen as the value within three complete stable periods before the arrival of the secondary reflection wave. The numerical data processing technique is similar to that described for the experimental investigation. However, p and v_c did not need phase matching, as there was no acquisition delay in the numerical simulations.

The horizontal wave force on the OWC model was also considered in this study. Fig. 9 illustrates the components of the horizontal force applied to the OWC model. F_{x1}, F_{x2} and F_{xb} are the horizontal forces applied to the structure by waves, while F_{xo1} and F_{xo2} are the horizontal forces recorded by the load cells. In the experiments, the total horizontal wave force acting on the OWC model can be calculated by adding the two horizontal wave force components F_{xo1} and F_{xo2} measured by load cells F2 and F3, respectively. Subsequently, a time history of the total wave force was plotted and averaged by computing half of the difference between the upper and lower envelopes. The averaged range selected was three complete stable periods, corresponding to the time-frame when P_a was processed. This yielded the amplitude of

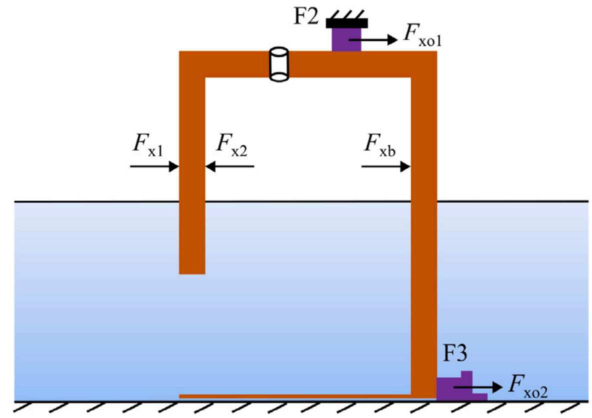

Fig. 9. Components of the horizontal force on the OWC structure.

the total horizontal wave force. In the following text, all expressions related to the force magnitude refer to its amplitude. In the numerical simulations, the horizontal force F_{xb} acting on the back wall, F_{x1} and F_{x2} acting on the seaward and shoreward surfaces of the front wall respectively can be obtained through integration. The horizontal forces on the front wall F_x and the full model F_{xo} can be calculated from:

$$F_x \boldsymbol{i} = F_{x1}\boldsymbol{i} - F_{x2}\boldsymbol{i} \tag{27}$$

$$F_{xo}\boldsymbol{i} = F_{x1}\boldsymbol{i} - F_{x2}\boldsymbol{i} + F_{xb}\boldsymbol{i} = F_{xo1}\boldsymbol{i} + F_{xo2}\boldsymbol{i} \tag{28}$$

where $\boldsymbol{i}$ is the unit vector in the positive x direction.

The wave energy converter can also serve as a breakwater in the present work. Hence, it is necessary to study the wave reflection coefficient K_r and the wave dissipation coefficient K_d, which can be denoted as:

$$K_r = \frac{H_r}{H_i} \tag{29}$$

$$K_d = 1 - K_r^2 - \xi \tag{30}$$

where H_r is the reflected wave height, which can be obtained based on the two-point method using data from any two wave gauges G2, G3 and G4. K_r was taken as the average of the three possible values.

3. Results and discussions

3.1. Model verification and validation

The mesh convergence tests for the numerical models and the comparison between experimental and numerical results are presented in this subsection. In all convergence and validation studies, the incident wave height is maintained at 0.05 m. In addition, the porosity of the porous plate is set to 10%, and the gap distance L between the porous plate and the front wall of the OWC model is 0.05 m.

The mesh resolutions of the OWC model and the porous plate model are investigated as the basis for the verification study of the integrated porous plate-OWC model. The mesh near the wave surface and at the OWC model is appropriately refined, especially the grid cells around the air orifice. This is due to the required accuracy to capture the air flow on a very small scale. The width of the porous plate is represented by 8, 16 and 32 cells in the x direction according to the level of mesh refinement. Based on the consideration of computational costs and numerical accuracy, the number of cells within the width of a porous plate is maintained at 16 in all subsequent numerical simulations. The details of mesh convergence tests and model validations for the integrated porous plate-OWC model are presented, with H_i = 0.05 m and λ = 1.9 m. Fig. 10 shows three mesh resolutions and the number

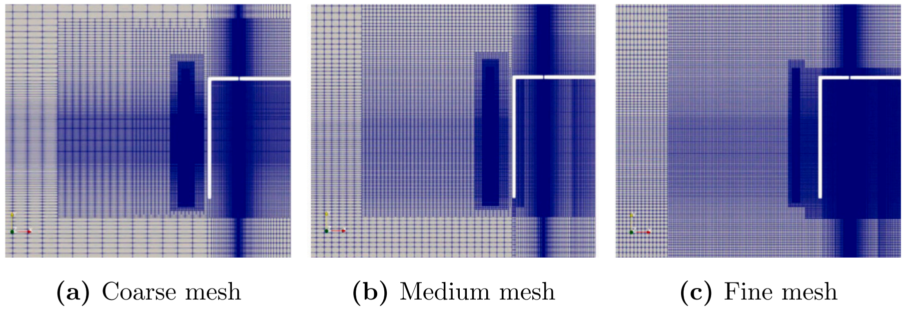

Fig. 10. Integrated porous plate-OWC model mesh with different levels of refinement.

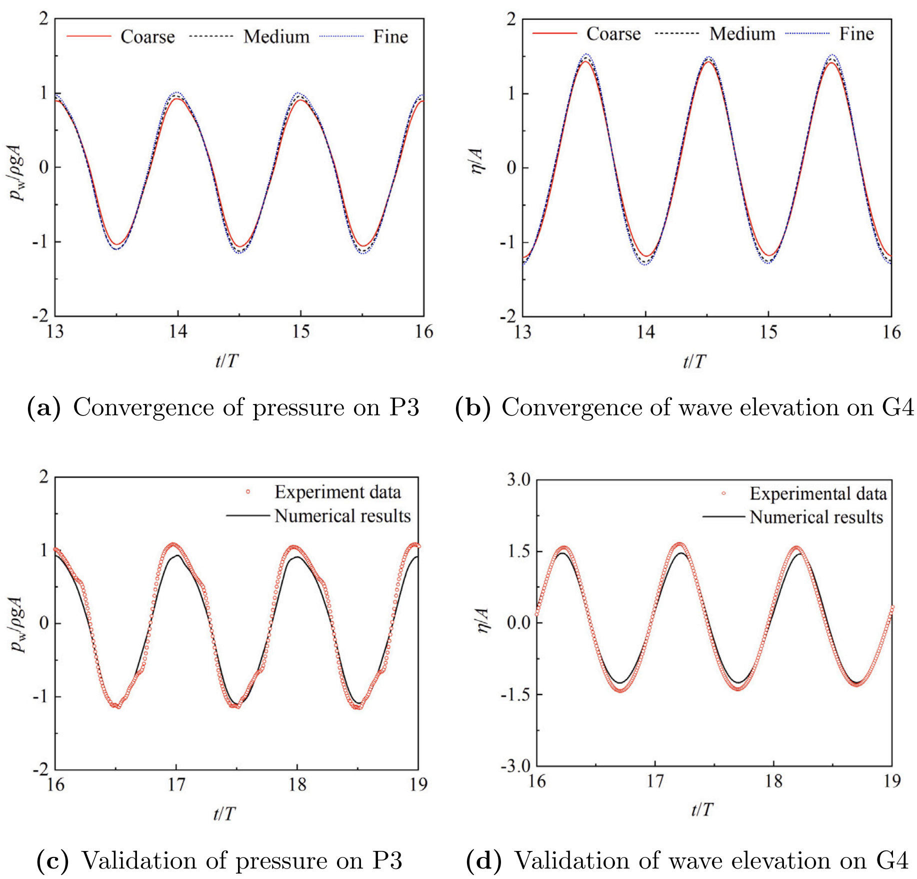

Fig. 11. Mesh convergence and validation tests for an integrated porous plate-OWC model with wave height H_i = 0.05 m and wavelength λ = 1.9 m.

of cells increases from 119 811 to 225 296. Fig. 11(a) and (b) show a comparison of the results of the hydrodynamic pressure on P3 and the wave surface elevation at G4 for different mesh resolutions. The results demonstrate that the medium mesh can achieve sufficient accuracy. Furthermore, these time histories obtained using the medium mesh are in good agreement with the corresponding experimental data, as shown in Fig. 11(c) and (d). In addition, Table 4 lists the Root Mean Square Error (RMSE) between numerical and experimental results at different mesh resolutions. Fig. 12 shows the variation of free surface elevations in the vicinity of the air chamber during a single typical wave period when λ = 1.2 m, and the numerical results are highly consistent with the experimental snapshots. Considering the computational efficiency and accuracy, the medium mesh resolution is adopted in the subsequent research.

Table 4
Number of cells and RMSE of the integrated porous plate-OWC model with different mesh resolutions.

Refine level	Number of cells	RMSE of $p_w/\rho gA$	RMSE of η/A
Coarse	119 811	0.164	0.16736
Medium	129 103	0.135	0.13202
Fine	225 296	0.114	0.12304

The above model verifications and validation studies are conducted using a single wave condition. A series of more comprehensive comparisons are presented in Figs. 13–15. According to the selected mesh resolution, the wave energy conversion efficiencies, dimensionless horizontal forces and wave reflection coefficients calculated using the numerical model are compared with the experimental data. The results

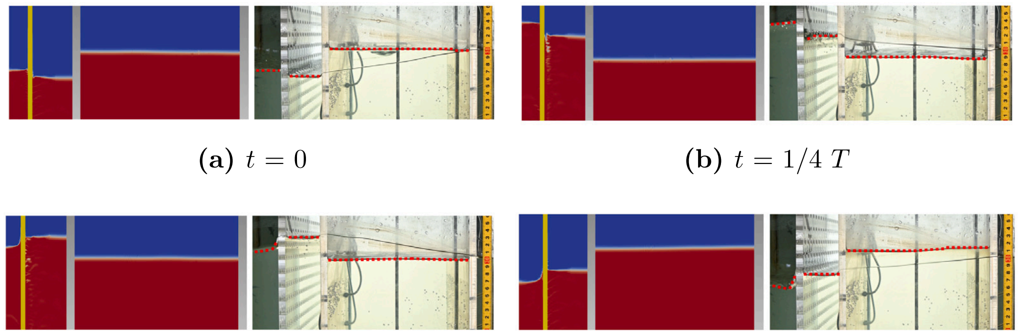

(a) $t = 0$ (b) $t = 1/4\ T$

(c) $t = 1/2\ T$ (d) $t = 3/4\ T$

Fig. 12. Comparisons of free surface elevations in the vicinity of the air chamber of the integrated porous plate-OWC model between the numerical results and the experimental data at: H_i = 0.05 m and λ = 1.2 m.

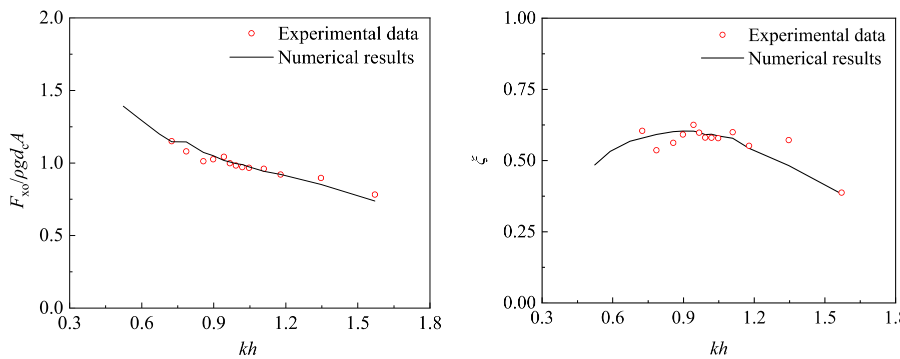

(a) Dimensionless horizontal force (b) Wave energy conversion efficiency

Fig. 13. Comparison of the dimensionless horizontal force and wave energy conversion efficiency between the OWC model and the experimental results with wave height H_i = 0.05 m (no porous plate present).

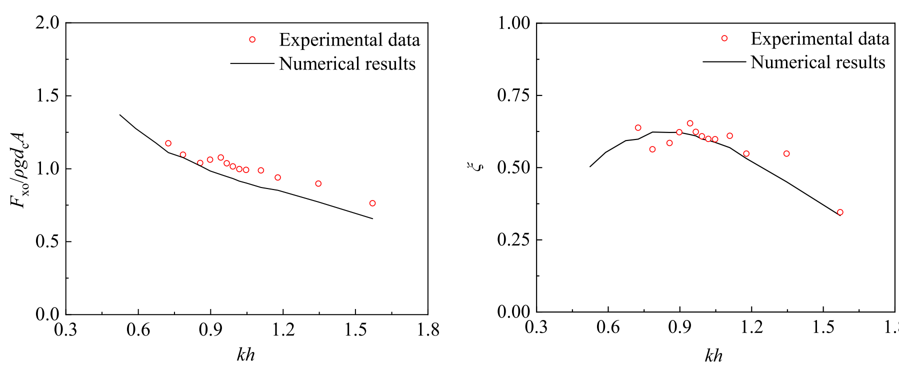

(a) Dimensionless horizontal force (b) Wave energy conversion efficiency

Fig. 14. Comparison of the dimensionless horizontal force and wave energy conversion efficiency between the integrated porous plate-OWC model and the experimental results with wave height H_i = 0.05 m.

show that the numerical models can accurately represent the hydrodynamic performance of different structures at all wave frequencies considered.

3.2. Selection of porosity and position of the porous plate

In this subsection, the appropriate porosity of the porous plate and its optimal spacing from the front wall of the OWC device are analyzed. This enables the further investigation of the hydrodynamic characteristics of the OWC device in Sections 3.3 and 3.4. It has previously been demonstrated that the front wall of a typical land-fixed OWC device is more susceptible to damage than the back wall (Medina-Lopez et al., 2015). Moreover, the horizontal forces on the front wall are much greater than the vertical forces (Wang et al., 2020). Therefore, for simplicity, the subsequent load analysis will focus on the horizontal forces on the front wall. In Fig. 16, the distance L between the porous plate and the front wall of the OWC device is maintained at 0.05 m, and the wave height H_i is kept at 0.05 m. Fig. 16(a) shows that the horizontal load F_x remains relatively stable with the variation in dimensionless wave number kh, when the porous plate is not integrated

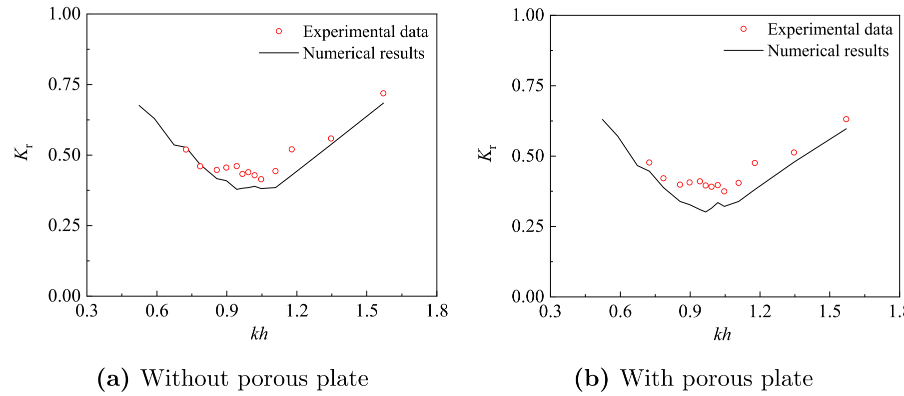

Fig. 15. Comparison of the wave reflection coefficient between the OWC model and the experimental results with and without the porous plate, wave height H_i = 0.03 m.

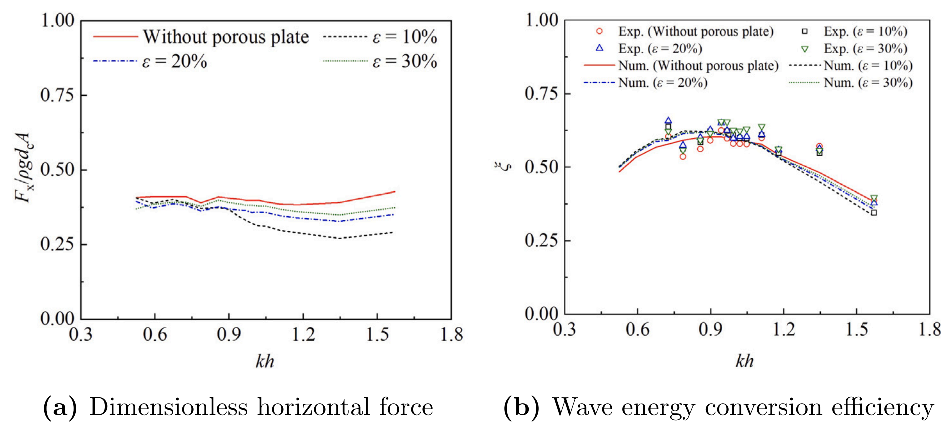

Fig. 16. Influence of porosity of the porous plate on (a) dimensionless horizontal force applied to the front wall and (b) the wave energy conversion efficiency.

with the OWC device. With the decrease in porosity ε, F_x gradually reduces, especially under high-frequency short wave conditions. The change in F_x can be explained by Eqs. (10) and (11): f is inversely proportional to ε, and the water wave pressure drop ΔP across the porous plate is directly proportional to f. Hence, the wave energy at the leeward side of the porous plate will decrease accordingly when ε decreases.

However, this does not imply that a lower porosity is necessarily better in all conditions, as it may lead to reduce energy capturing efficiency of the OWC device. As shown in Fig. 16(b), the wave energy conversion efficiency ξ first increases and then decreases with increasing kh. In the low-frequency region, the variation of ξ is not particularly sensitive to the three levels of porosity. When the wave frequency is high, it can be observed that a decrease in porosity causes a gradual reduction in efficiency. It is worth mentioning that the influence of the porous plate on the efficiency is related to the incident wave frequency. In the high-frequency band, the porous plate has a negative influence on the wave energy conversion efficiency, which is to be expected. As the wave frequency decreases, the efficiency of the OWC device integrated with the porous plate is higher than that without the plate. The mechanism behind this interesting phenomenon will be elucidated in Section 3.4. Based on the above results, and within the parameter range of this study, the porous plate with ε = 10% can achieve the best wave energy dissipation. The reduction in the wave energy conversion efficiency at high wave frequencies does not exceed 11%, and in low-frequency wave conditions, the efficiency can increase by up to 6%. Therefore, in the following research, the porosity of the porous plate will be maintained at 10%.

The position of the porous plate, specifically its distance from the front wall, has a large influence on the hydrodynamic performance of the OWC device. As illustrated in Fig. 17(a), in high-frequency incident wave conditions, there is a marked decrease in the horizontal force on the front wall, as the relative spacing L/b increases from 0.125 to 0.25. However, a further increase in relative spacing does not elicit the same large load-reduction effect. As the dimensionless wave frequency kh decreases, the effect of the relative spacing on the horizontal force gradually stabilizes. In fact, the gap between the porous plate and the front wall creates an area where the incident and reflected waves repeatedly stack and dissipate energy. When the gap is increased, more wave energy is dissipated, resulting in reduced horizontal forces. Nevertheless, if the porous plate is positioned too far away from the OWC device, its relative effect will no longer be significant. Fig. 17(b) shows that the wave energy conversion efficiency under high-frequency waves continuously decreases with increasing L/b. This observation supports the finding that the porous plate should be installed at a suitable distance from the OWC device, so as to effectively reduce the horizontal force on the front wall while minimizing the loss of efficiency. Therefore, after a comprehensive analysis, the relative spacing between the porous plate and the front wall of the OWC device is set to 0.25 in the following analyses.

It is worth mentioning that both Figs. 16 and 17 show that in the high-frequency region, decrements in the hydrodynamic efficiency of the OWC device after integrating the porous plate are always smaller than those in the relating horizontal force. The reason for this behavior is that some of the wave energy dissipated by the porous plate does not contribute to the hydrodynamic efficiency in the first place. Fig. 18 shows the numerical comparison of the wave pressure, air pressure and air flow rate with and without the porous plate, with the wave height H_i = 0.07 m and wavelength λ = 1.2 m. Although the addition of the porous plate resulted in decreases in all three physical

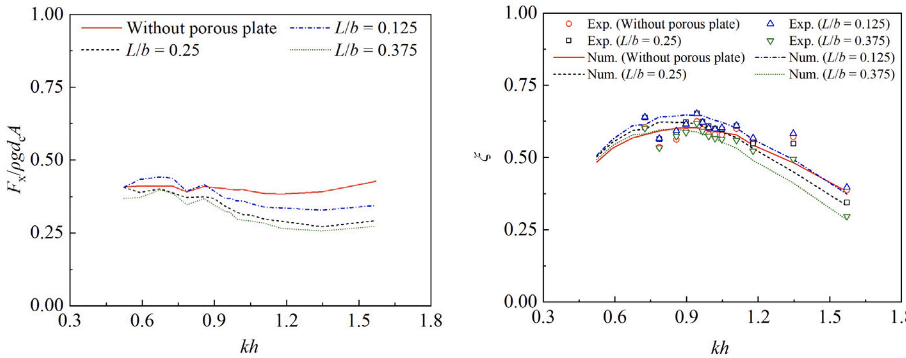

(a) Dimensionless horizontal force (b) Wave energy conversion efficiency

Fig. 17. Influence of the porous plate position on (a) dimensionless horizontal force applied to the front wall and (b) the wave energy conversion efficiency.

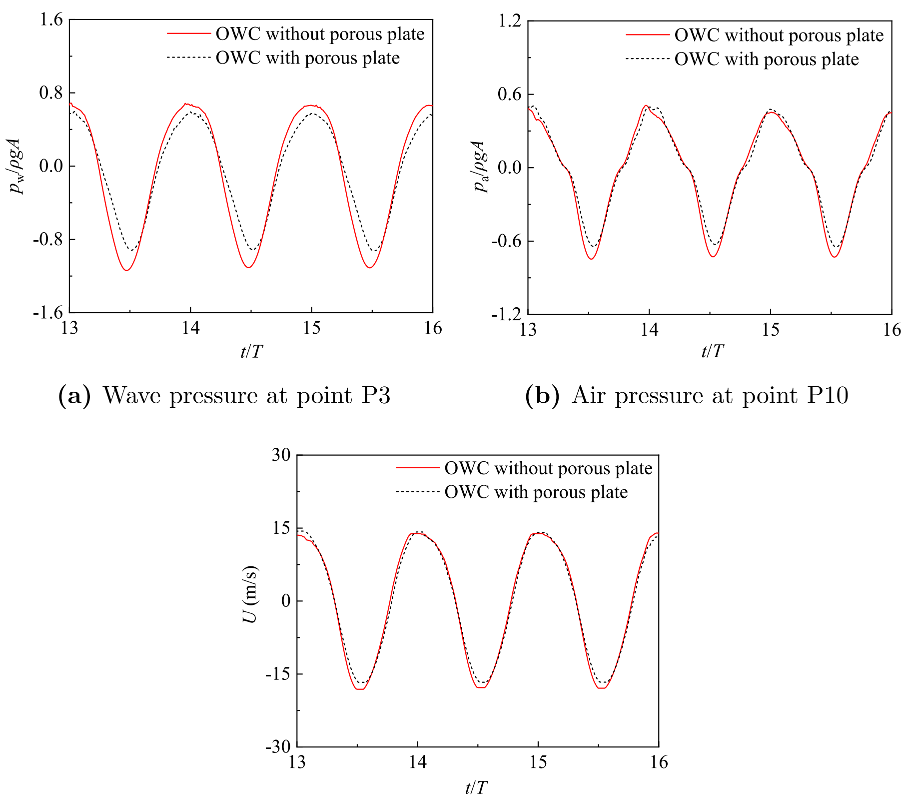

(a) Wave pressure at point P3 (b) Air pressure at point P10

(c) Air flow rate at the air orifice

Fig. 18. Comparison of the wave pressure, air pressure, and air flow rate with and without the porous plate with wave height H_i = 0.07 m and wavelength λ = 1.2 m.

parameters mentioned above, the reduction in wave pressure on the front wall is significantly greater than the latter two. This is because the high-frequency wave energy weakened by the porous plate has low penetrability into the OWC chamber even in the absence of the porous plate, so the decreases in air pressure and air flow rate inside the chamber are relatively small.

3.3. Characteristics of horizontal forces

The underlying mechanism of horizontal force application on the front wall is systematically investigated and elucidated, especially the influence of wave nonlinearity. Fig. 19 shows that when the incident wave height H_i increases from 0.03 m to 0.1 m, the porous plate can consistently reduce the horizontal force in the high wave-frequency region. It is particularly noteworthy that the influence of the porous plate becomes increasingly effectual as the wave height amplifies. Specifically, the porous plate can reduce the horizontal force by up to 20% at H_i = 0.03 m. When the incident wave height increases to 0.1 m, this value rises to 52%. This performance is due to the fact that the large wave height generates strong wave nonlinearity with many high-frequency components. Combined with the strong energy damping ability of the porous plate in high-frequency waves, a higher proportion of wave energy is dissipated at high wave heights compared to that at small wave heights. Therefore, the integration of the porous plate can play a crucial role in improving the survivability of the OWC device in extreme sea conditions with high wave amplitudes. In addition, as the wave frequency decreases, the horizontal force magnitudes on the front wall in the integrated system trend toward the values before integration. This phenomenon can be explained by Fig. 20.

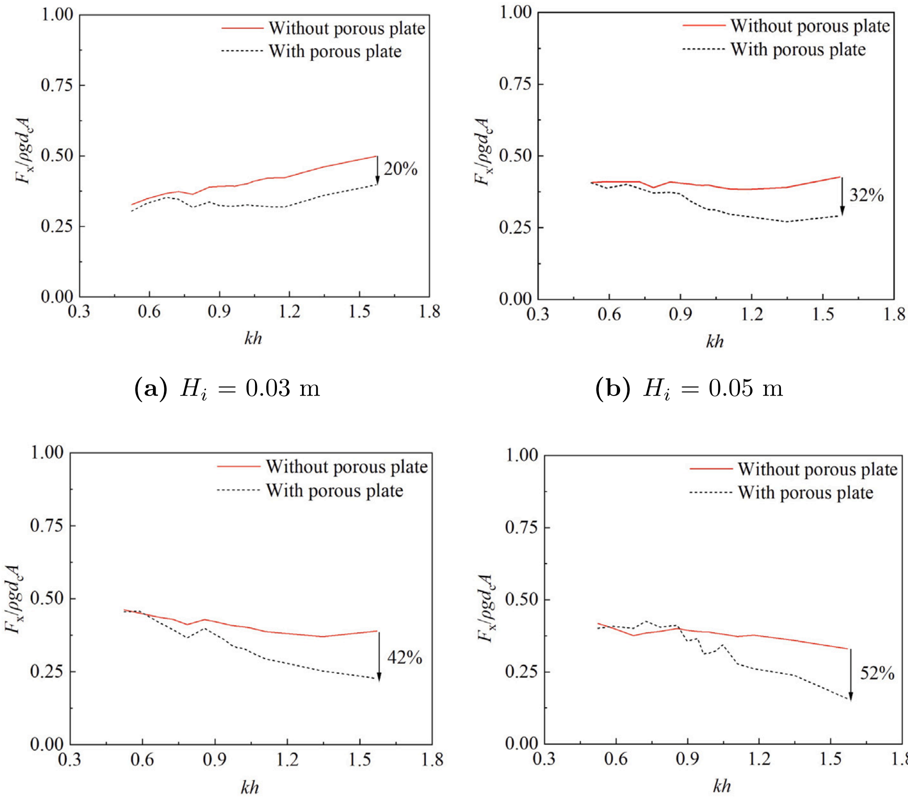

(a) $H_i = 0.03$ m (b) $H_i = 0.05$ m

(c) $H_i = 0.07$ m (d) $H_i = 0.1$ m

Fig. 19. Comparison of dimensionless horizontal forces applied to the front wall of the OWC device as a function of varying wave nonlinearity.

Fig. 20 illustrates the variation in the horizontal forces on the seaward and shoreward surfaces of the front wall of the OWC device. Both components of the horizontal force increase monotonically with decreasing kh, and the porous plate has a greater effect on the seaward surface component of the horizontal force. In the high-frequency region, the horizontal resultant force on the front wall has decreased significantly, as shown in Fig. 19. This is due to the relatively large reduction of the seaward surface force component and the smaller variation in the shoreward surface force component. However, as the wave frequency decreases, the magnitude of the decrease in the seaward surface force component gradually trends towards zero in cases with $H_i = 0.03$ m and 0.05 m. As a result, the total horizontal forces before and after integrating the porous plate are almost identical. When $H_i =$ 0.07 m or 0.1 m, the increase in the shoreward surface force component offsets the decline in the seaward component, which leads to the total horizontal force attaining a value similar to that before the integration of the porous plate. In summary, the porous plate generally reduces the horizontal force on the front wall by reducing the seaward component, and this effect diminishes with the decrease of wave frequency.

Fig. 20 also shows that the force component F_{x2} is generally greater than F_{x1}. Fig. 21(a) illustrates this point with $H_i = 0.05$ m and $\lambda =$ 1.9 m. However, at the same time, the wave run-up heights on the seaward surface are much higher than those on the shoreward surface. An example is shown in Fig. 21(b). This behavior seems contradictory and its explanation lies in the effect of air pressure, which is shown in the comparison between Fig. 21(c) and (d). The seaward surface of the front wall is always exposed to the atmosphere, so the air pressure remains relatively stable, that is, the applied air force on the surface can be neglected, as shown in Fig. 21(c). In contrast, the shoreward surface is located inside the air chamber with high air pressure, and the pneumatic force accounts for a large proportion of the total force applied to the wall, as indicated in Fig. 21(d). Consequently, although the wave load on the shoreward surface is smaller than the seaward surface, the total internal force composed of the pneumatic force and the wave force is larger than that at the exterior surface.

Considering Figs. 19 and 20, it can be observed that although the difference between F_{x1} and F_{x2} apparently changes with the variation of wave frequency, the total horizontal force F_x only fluctuates slightly when there is no porous plate. Fig. 22 clearly reveals this behavior using two simulation cases with $\lambda = 1.2$, 3.6 m, and $H_i = 0.05$ m. The wave peak of F_{x2} appears after the wave trough of F_{x1} when the wavelength is 1.2 m, while the former appears before the latter as the wavelength increases to 3.6 m. This demonstrates that the relative phase of F_{x1} and F_{x2} change with the wave frequency. As a result of the superposition of F_{x1} and F_{x2}, the total F_x is greatly influenced by the relative phase. Although both seaward and shoreward force components have increased from $\lambda = 1.2$ m to $\lambda = 3.6$ m, the difference in relative phase effectively changes the time histories of F_x and weakens the influence of the variation of F_{x1} and F_{x2}.

Fig. 23 explains why F_{x2} becomes larger after integrating the porous plate under small kh conditions compared to before integration, as shown in Fig. 20. Considering the hydrodynamic pressure at point P6 with $H_i = 0.07$ m and $\lambda = 2.6$ m as an example, it can be seen that the addition of a porous plate slightly increases the first-order harmonic component of the hydrodynamic pressure at point P6. Generally, when water waves interact with the OWC device, wave energy will transfer from the first-order wave to the second-order harmonic waves (Wang et al., 2018). These second-order harmonic waves are reflected from the front wall of the chamber, leaving the remaining first-order waves to enter the chamber. However, the porous plate now hinders the process of wave energy transition from first order to higher orders, resulting in additional first-order wave energy entering the chamber and generating the larger hydrodynamic pressure. This process will be further analyzed

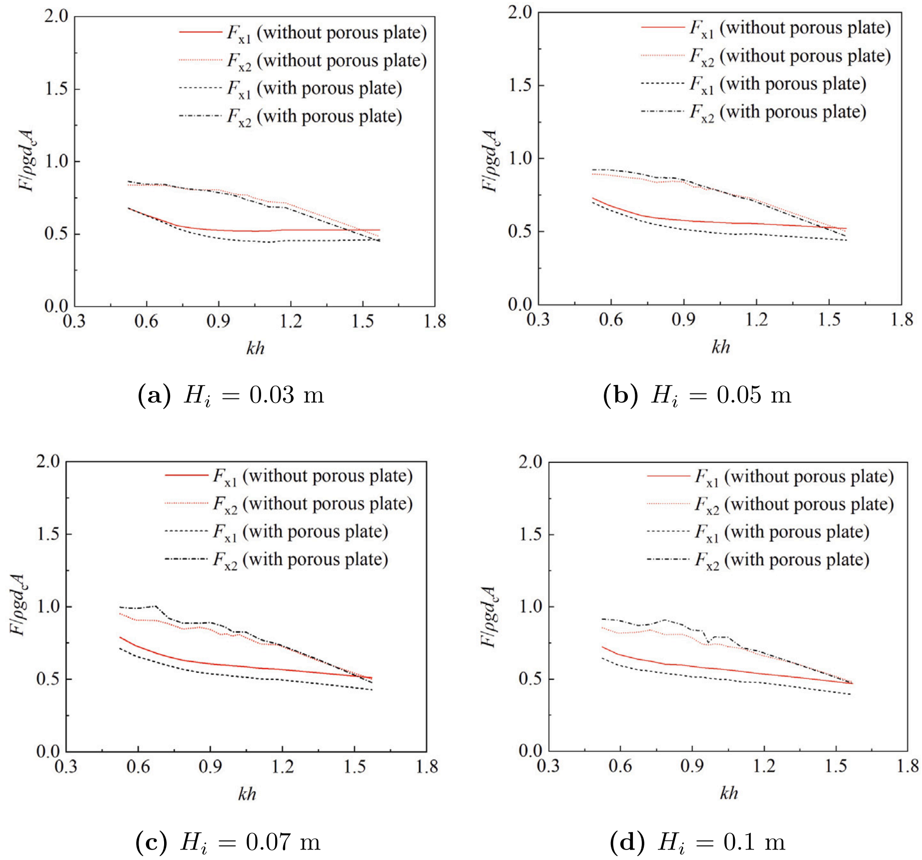

Fig. 20. Comparison of dimensionless horizontal forces applied to the seaward and shoreward surfaces of the front wall as a function of varying wave nonlinearity.

in the next section from the perspective of wave energy conversion and wave reflection.

3.4. Wave energy conversion, reflection and dissipation

In addition to the forces applied to an OWC device, wave energy conversion efficiency and the wave reflection coefficient are important hydrodynamic performance indicators of an OWC device. Fig. 24 shows that the wave energy conversion efficiency first increases to a peak value and then gradually decreases with increasing kh. This is because when the wave frequency is very low, the incident wavelength is correspondingly long and the wave energy entering the chamber is miniscule. As the wavelength shortens, the proportion of wave energy entering the chamber increases until it reaches its maximum. Thereafter, as the wavelength continues to shorten, the waves are more easily reflected at the front wall and the wave energy conversion efficiency is significantly reduced. It is notable that the peak efficiency decreases as the incident wave height increases. This can be explained due to the fact that more high-order harmonic wave components are reflected when the wave nonlinearity increases, making it difficult for the wave energy to be absorbed by the OWC device. Furthermore, Fig. 24 shows that after the addition of the porous plate, the wave energy conversion efficiency is slightly lower at high wave frequencies, but gradually reaches, and even exceeds the original value at low wave frequencies. The above phenomenon is more perceptible under strong wave nonlinearity. This can be attributed to two opposite effects of the porous plate. On the one hand, the porous plate weakens the transfer of wave energy from low frequency to high frequency as mentioned in Section 3.3, which is beneficial for more first-order wave energy to enter the chamber. On the other hand, the area formed between the porous plate and the front wall of the OWC device promotes the dissipation of wave energy, due to the complex interaction of incident and reflected waves. When the wave frequency is high, the wave energy dissipation is greater than the increase of the first-order component of wave energy, so the energy conversion efficiency is lower than that before integrating the porous plate. As the wave frequency decreases, the increase in first-order wave energy exceeds the dissipating effect of the porous plate, leading to an improvement in efficiency.

Taking the case of wave height $H_i = 0.07$ m and wavelength $\lambda = 2.6$ m as an example. Fig. 25(a) and (b) show the changes in air pressure time histories after the addition of the porous plate and the increase in the amplitude of the first-order component respectively. Fig. 25(c) and (d) demonstrate that the porous plate also helps to enhance the first-order wave elevation in the chamber. These improvements collectively lead to an increase in the wave energy conversion efficiency. Moreover, as indicated in Fig. 25(e) and (f), the wave run-up on the seaward surface of the front wall is markedly reduced after integrating the porous plate. In particular, there is a dramatic decrease in the second-order harmonic component of the wave run-up. This further confirms that the transfer of wave energy to higher order components outside the chamber is reduced, resulting in an increase in the first order wave energy that can more easily enter the chamber.

As a breakwater-type wave energy converter, the wave reflection and dissipation coefficients are important parameters for determining the wave energy dissipation capacity of the OWC structure. Fig. 26 shows that the system with a porous plate can effectively reduce the wave reflection coefficient and increase the dissipation coefficient at various wave frequencies, using wave height $H_i = 0.03$ m as an example. This is due to the wave energy dissipation characteristics of the porous plate, as discussed above. When the wave frequency tends towards the high or low band, the increased wave reflection and reduced wave dissipation can be presented. The minimum reflection coefficient, maximum dissipation coefficient and wave energy conversion efficiency occur in the same wave frequency band. Furthermore,

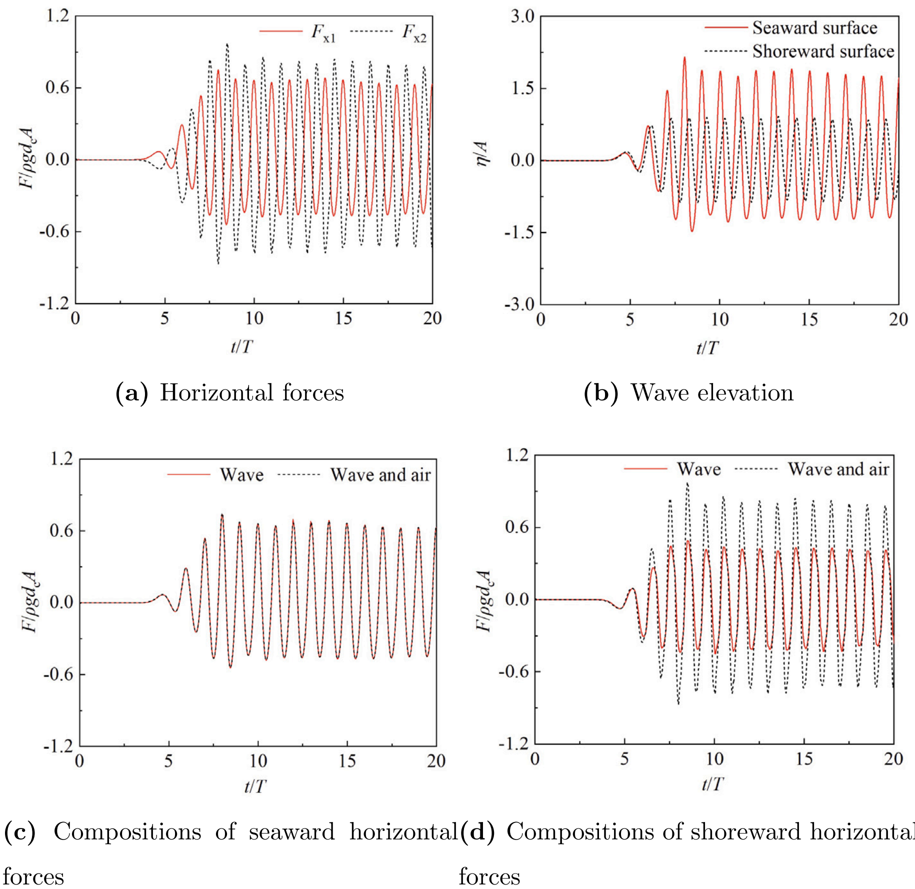

(a) Horizontal forces (b) Wave elevation

(c) Compositions of seaward horizontal forces (d) Compositions of shoreward horizontal forces

Fig. 21. Decomposition of dimensionless horizontal forces applied to the seaward and shoreward surfaces of the front wall for wavelength λ = 1.9 m and wave height H_i = 0.05 m.

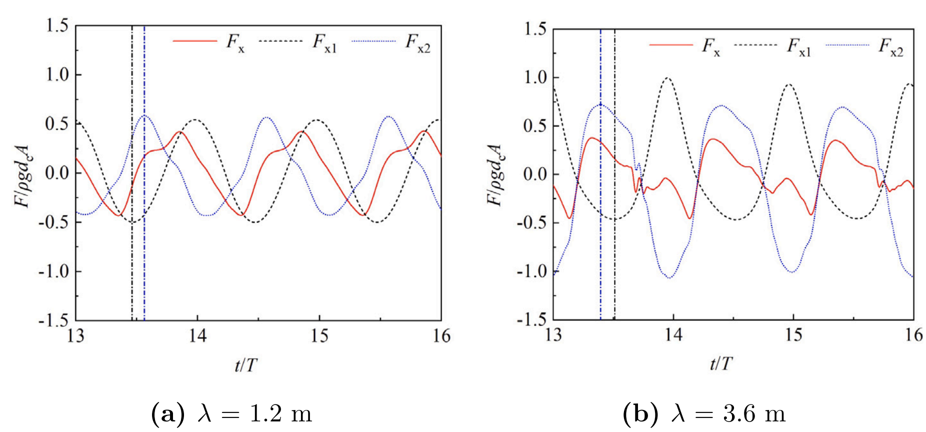

(a) $\lambda = 1.2$ m (b) $\lambda = 3.6$ m

Fig. 22. Comparison of the relative phases of the dimensionless horizontal force components under wavelength λ = 1.2 m (a) and 3.6 m (b), with wave height H_i = 0.05 m (The black vertical line represents the position of the wave trough of F_{x1}, and the blue vertical line represents the position of the wave peak of F_{x2}).

based on Table 5, it can be seen that the reflection coefficient is decreased by up to 21.139% and an average decrease of 14.614% is achieved after adding the porous plate. The dissipation coefficient is increased by a maximum of 186.129%, with an average increase of 67.164%. In summary, the slight loss of wave energy conversion efficiency caused by the porous plate is confined to the high-frequency wave region, and in the low-frequency region, the porous plate is beneficial for improving conversion efficiency. In addition, the porous plate helps reduce the reflection coefficient and significantly increase the dissipation coefficient throughout the entire wave frequency range.

4. Conclusions

In the present work, a land-fixed breakwater-type wave energy converter combining an OWC device and a porous plate was considered, and its hydrodynamic performance was investigated. A series of systematic physical experiments and numerical simulations based on the Computational Fluid Dynamics technique were conducted simultaneously to verify and validate the results. The macroscopic porous modeling approach was used to simplify the simulation of the interaction between the waves and a porous plate. By changing the porosity of the porous plate, and its distance to the front wall of the OWC device, as

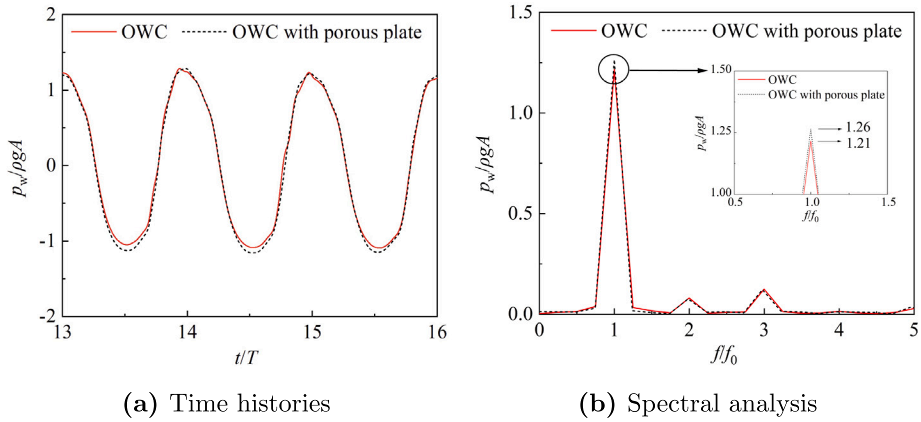

Fig. 23. Influence of the porous plate on the dimensionless hydrodynamic pressure at point P6 for wavelength λ = 2.6 m and wave height H_i = 0.07 m.

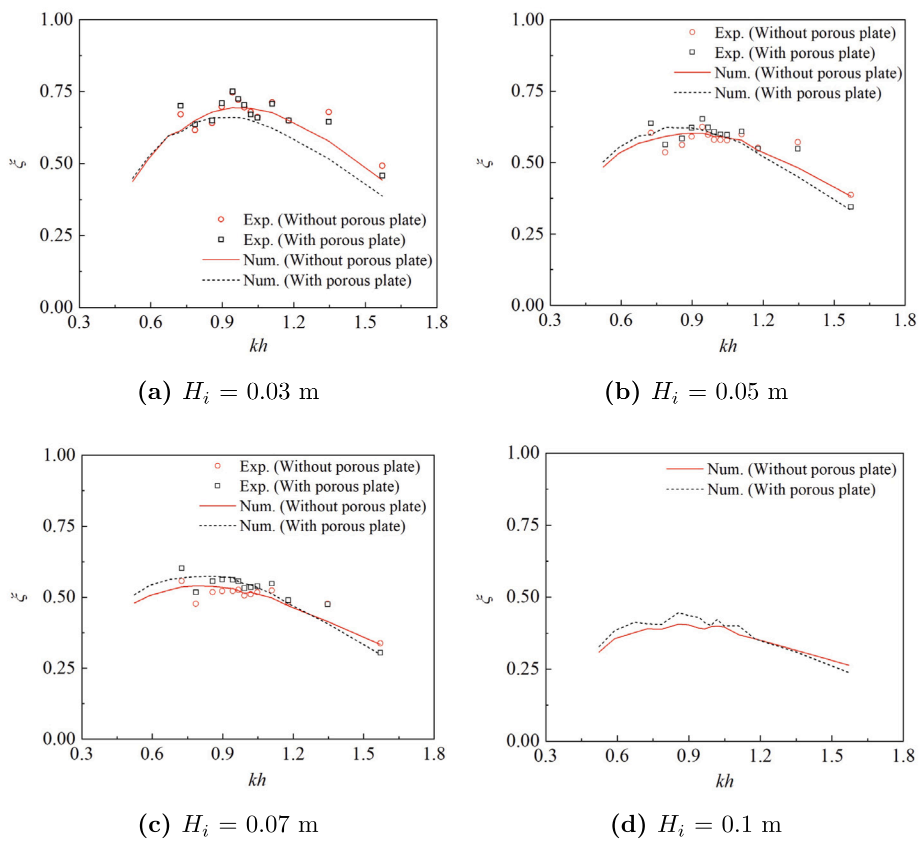

Fig. 24. Comparison of the wave energy conversion efficiency of the OWC device under different wave nonlinearities.

well as varying the wave nonlinearity, the mechanisms of the horizontal force application on the OWC device and the wave energy conversion, reflection and dissipation were analyzed in detail. The following main conclusions can be drawn:

When the wave frequency is high, small porosity and large gap spacing enhance the effect of the porous plate to reduce the horizontal force on the front wall significantly. However, this also leads to a slight decrease in the wave energy conversion efficiency. Because the dissipating effect of the porous plate on water wave energy is dominant in the high-frequency region, there is little change in the hydrodynamic performance of the wave energy converter at low wave frequencies. In summary, selecting an appropriate porosity and gap spacing, according to engineering requirements, can effectively reduce the economic cost of the wave energy converter and prolong its design life.

The porous plate has a more notable effect in reducing horizontal forces in highly nonlinear wave conditions and can reduce them by up to 52%. The horizontal forces on the seaward surface of the front wall are generally reduced after the porous plate is integrated, whereas the shoreward horizontal forces gradually increase as the wave frequency decreases. The reason for the latter behavior is that the porous plate hinders the transfer of energy from first-order waves to second-order harmonic waves, thereby allowing more first-order wave energy to enter the chamber. Therefore, considering the influences of the porous plate on the horizontal forces in the seaward and shoreward surfaces, the total horizontal forces on the front wall under low-frequency conditions are similar in magnitude to the cases without the porous plate.

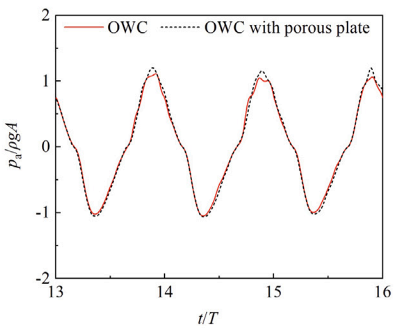

(a) Time histories of the air pressure

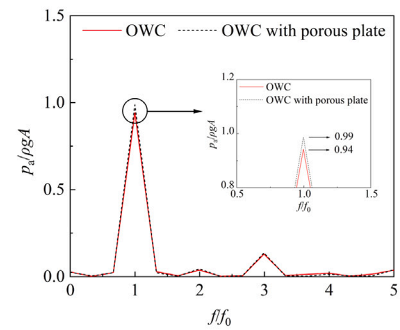

(b) Spectral analysis of the air pressure

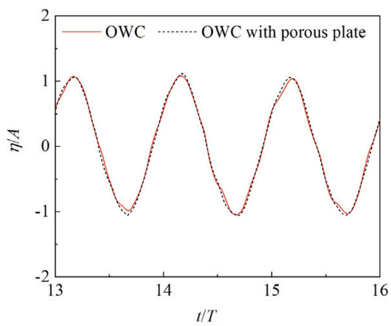

(c) Time histories of the internal wave elevation

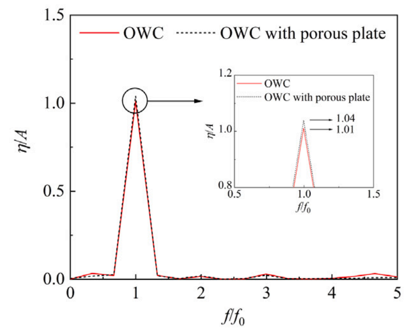

(d) Spectral analysis of the internal wave elevation

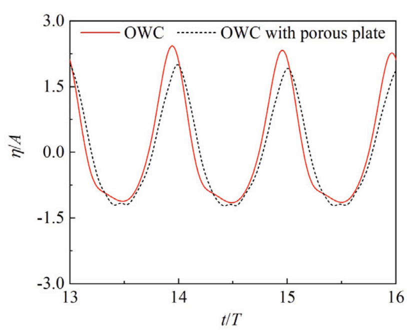

(e) Time histories of the external wave elevation

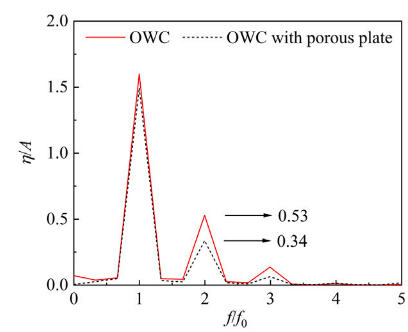

(f) Spectral analysis of the external wave elevation

Fig. 25. Influence of the porous plate on the dimensionless air pressure, internal and external wave elevation at the chamber for wavelength λ = 2.6 m and wave height H_i = 0.07 m.

Although the wave energy conversion efficiencies are slightly reduced due to the integration of the porous plate at high frequency wave conditions, the efficiencies can exceed the original values at low wave frequencies, which is particularly evident at high wave heights. This is attributed to two main effects caused by the porous plate: one is to increase the first-order waves entering the chamber while reducing the second-order waves outside the chamber; the other is to increase the dissipation of wave energy in front of the OWC device. This study demonstrated that the former effect is stronger than the latter when the wave frequency is low, resulting in an increase in efficiency, and vice versa. Furthermore, the wave reflection coefficients are reduced to a certain extent by the porous plate, and the wave dissipation coefficients are significantly increased at the same time.

In a future study, the performance of this wave energy converter will be investigated in realistic sea-states including random waves, in addition to expanding the numerical and experimental models from two dimensions to three dimensions. Due to the sub- and super-harmonic interactions in three-dimensional nonlinear irregular waves, more complex variations may emerge in terms of the wave loads and wave energy absorbed by the OWC device (Romolo and Arena, 2013; Romolo et al., 2014, 2024). It is necessary to conduct a comprehensive investigation into the reliability and consistency of the performance of this proposed OWC device integrated with a porous plate in various real sea-state wave environments. On this basis, real scale numerical and physical models will be established to investigate the actual power generation capacity and hydrodynamic performance of the OWC device integrated

Table 5
Changes of the wave reflection and dissipation coefficients with and without porous plate.

Wave length (m)	*kh*	K_r (Without porous plate)	K_r (With porous plate)	Reduce percentage	K_d (Without porous plate)	K_d (With porous plate)	Increase percentage
3.6	0.5236	0.67557	0.62984	6.768%	0.10528	0.1539	46.181%
3.2	0.58905	0.62957	0.57036	9.405%	0.08883	0.15262	71.813%
2.8	0.6732	0.5358	0.46605	13.018%	0.11663	0.18692	60.266%
2.6	0.72498	0.52767	0.44627	15.425%	0.10676	0.19153	79.406%
2.4	0.7854	0.46647	0.38811	16.797%	0.1325	0.20733	56.473%
2.2	0.8568	0.41663	0.33903	18.626%	0.14747	0.22615	53.348%
2.1	0.8976	0.40927	0.32773	19.922%	0.14638	0.23376	59.695%
2.0	0.94248	0.37873	0.30986	18.185%	0.16204	0.24362	50.347%
1.95	0.96664	0.38267	0.30178	21.139%	0.16093	0.2494	54.981%
1.9	0.99208	0.38503	0.3151	18.164%	0.15882	0.24395	53.609%
1.85	1.01889	0.3895	0.33516	13.952%	0.15596	0.2371	52.028%
1.8	1.0472	0.3814	0.32131	15.756%	0.16786	0.25472	51.744%
1.7	1.1088	0.38493	0.33897	11.942%	0.17436	0.26188	50.196%
1.6	1.1781	0.42887	0.38139	11.069%	0.16625	0.26094	56.956%
1.4	1.3464	0.53773	0.47872	10.974%	0.13288	0.2544	91.447%
1.2	1.5708	0.684	0.5972	12.69%	0.08924	0.25535	186.129%

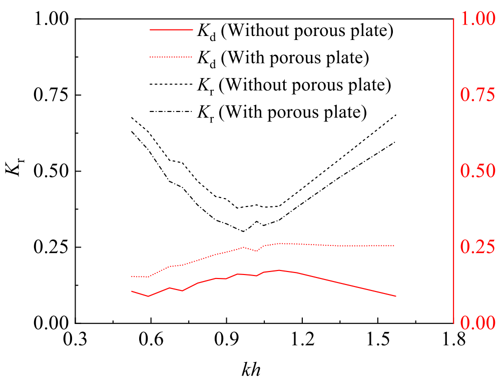

Fig. 26. Influence of the porous plate on the wave reflection coefficient and dissipation coefficient.

with a porous plate. This full-scale study will permit an evaluation of the performance of the protective porous plate in real sea conditions. A detailed analysis of the influence of scale changes, including air compressibility, will be conducted simultaneously in the future work.

CRediT authorship contribution statement

Qianze Zhuang: Writing – original draft, Validation, Software, Methodology, Investigation, Formal analysis. **Dezhi Ning:** Writing – review & editing, Supervision, Methodology, Funding acquisition, Conceptualization. **Robert Mayon:** Writing – review & editing, Funding acquisition. **Yu Zhou:** Writing – review & editing.

Declaration of competing interest

We confirm that this manuscript has not been published elsewhere and is not under consideration by another journal. All authors have approved the manuscript.

The authors declare no conflict of interest.

Data availability

Data will be made available on request.

Acknowledgments

This work is supported by the National Key R&D Program of China (Grant No. 2023YFB4204101), the National Natural Science Foundation of China (Grant Nos. U22A20242 and 52250410362), the China Postdoctoral Science Foundation (2024T170092).

References

Adcock, T.A., Draper, S., Willden, R.H., Vogel, C.R., 2021. The fluid mechanics of tidal stream energy conversion. Annu. Rev. Fluid Mech. 53, 287–310.
Elhanafi, A., Macfarlane, G., Ning, D., 2018. Hydrodynamic performance of single–chamber and dual–chamber offshore–stationary oscillating water column devices using CFD. Appl. Energy 228, 82–96.
Feichtner, A., Mackay, E., Tabor, G., Thies, P.R., Johanning, L., 2021a. Comparison of macro-scale porosity implementations for CFD modelling of wave interaction with thin porous structures. J. Marine Sci. Eng. 9 (2), 150.
Feichtner, A., Mackay, E., Tabor, G., Thies, P.R., Johanning, L., Ning, D., 2021b. Using a porous-media approach for CFD modelling of wave interaction with thin perforated structures. J. Ocean Eng. Mar. Energy 7, 1–23.
Fu, L., Wang, R., Ning, D., Mayon, R., 2023. Numerical investigation on the hydrodynamic performance of a land-based OWC system with multi-chamber modules. Appl. Ocean Res. 141, 103801.
Gayathri, R., Khan, M.B., Behera, H., Tsai, C.C., 2022. Wave attenuation by a submerged circular porous membrane. J. Ocean Eng. Sci..
Goda, Y., Suzuki, Y., 1977. Estimation of incident and reflected waves in random wave experiments. In: Coastal Engineering 1976. pp. 828–845.
Hirt, C.W., Nichols, B.D., 1981. Volume of fluid (VOF) method for the dynamics of free boundaries. J. Comput. Phys. 39 (1), 201–225.
Issa, R.I., 1986. Solution of the implicitly discretised fluid flow equations by operator-splitting. J. Comput. Phys. 62 (1), 40–65.
Jacobsen, N.G., Fuhrman, D.R., Fredsøe, J., 2012. A wave generation toolbox for the open-source CFD library: OpenFoam®. Int. J. Numer. Methods Fluids 70 (9), 1073–1088.
Kamath, A., Bihs, H., Arntsen, Ø.A., 2015. Numerical modeling of power take-off damping in an oscillating water column device. Int. J. Marine Energy 10, 1–16.
Kamranzad, B., Amarouche, K., Akpinar, A., 2022. Linking the long-term variability in global wave energy to swell climate and redefining suitable coasts for energy exploitation. Sci. Rep. 12 (1), 14692.
Larsen, B.E., Fuhrman, D.R., Roenby, J., 2019. Performance of interfoam on the simulation of progressive waves. Coast. Eng. J. 61 (3), 380–400.
Le Méhauté, B., 2013. An Introduction to Hydrodynamics and Water Waves. Springer Science & Business Media.
Li, J., Pan, S., Chen, Y., Yao, Y., Xu, C., 2022a. Assessment of combined wind and wave energy in the tropical cyclone affected region: An application in China seas. Energy 260, 125020.
Li, X., Zhang, W., 2019. 3D numerical simulation of wave transmission for low-crested and submerged breakwaters. Coast. Eng. 152, 103517.
Li, Y., Zhao, X., Geng, J., Mackay, E., Johanning, L., 2022b. Wave scattering by a vertical cylinder with a submerged porous plate: Further analysis. Ocean Eng. 259, 111711.
Li, Y., Zhao, X., Zou, Q., Geng, J., 2022c. Hydrodynamic performance of dual-chamber oscillating water column array under oblique waves. Phys. Fluids 34 (11), 117112.
Liu, Z., Xu, C., Kim, K., Zhang, X., Ning, D., 2024. Hydrodynamic and energy-harvesting performance of an isolated oscillating water column device: An experimental study. Coast. Eng. 189, 104459.
López, I., Andreu, J., Ceballos, S., De Alegría, I.M., Kortabarria, I., 2013. Review of wave energy technologies and the necessary power-equipment. Renew. Sustain. Energy Rev. 27, 413–434.
Mackay, E., Johanning, L., 2020. Comparison of analytical and numerical solutions for wave interaction with a vertical porous barrier. Ocean Eng. 199, 107032.
Martin, M.B., Pinon, G., Barajas, G., Lara, J.L., Reveillon, J., 2023. Computations of pressure loads on an oscillating water column with experimental comparison for random waves. Coast. Eng. 179, 104228.

Mayon, R., Ning, D., Sun, Y., Ding, Z., Wang, R., Zhou, Y., 2023. Experimental investigation on a novel and hyper-efficient oscillating water column wave energy converter coupled with a parabolic breakwater. Coast. Eng. 185, 104360.
Mayon, R., Ning, D., Zhang, C., Chen, L., Wang, R., 2021. Wave energy capture by an omnidirectional point sink oscillating water column system. Appl. Energy 304, 117795.
Mayon, R., Ning, D.Z., Zhang, C.W., Johanning, L., 2022. Hydrodynamic performance of a porous-type land-fixed oscillating water column wave energy converter. China Ocean Eng. 36 (1), 1–14.
Medina-Lopez, E., Allsop, W., Dimakopoulos, A., Bruce, T., 2015. Conjectures on the failure of the OWC breakwater at mutriku. In: Coastal Structures and Solutions To Coastal Disasters Joint Conference 2015. American Society of Civil Engineers Reston, VA, pp. 592–603.
Molin, B., 2011. Hydrodynamic modeling of perforated structures. Appl. Ocean Res. 33 (1), 1–11.
Ning, D.Z., Mu, D., Wang, R.Q., Mayon, R., 2023. Experimental and numerical investigations on the solitary wave actions on a land-fixed OWC wave energy converter. Energy 282, 128363.
Ning, D.Z., Wang, R.Q., Zou, Q.P., Teng, B., 2016. An experimental investigation of hydrodynamics of a fixed OWC wave energy converter. Appl. Energy 168, 636–648.
Ning, D.Z., Zhao, X.L., Teng, B., Johanning, L., 2017. Wave diffraction from a truncated cylinder with an upper porous sidewall and an inner column. Ocean Eng. 130, 471–481.
Pawitan, K.A., 2019. Wave Loadings and Scaling Effects On, and Within, an Oscillating Water Column (OWC) Caisson Breakwater (Ph.D. thesis). University of Edinburgh.
Pawitan, K.A., Dimakopoulos, A.S., Vicinanza, D., Allsop, W., Bruce, T., 2019. A loading model for an OWC caisson based upon large-scale measurements. Coast. Eng. 145, 1–20.
Poguluri, S.K., Kim, J., George, A., Cho, I.-H., 2022. Wave interaction with horizontal multilayer porous plates. J. Waterw. Port Coast. Ocean Eng. 148 (5), 04022016.
Qiao, D., Feng, C., Yan, J., Liang, H., Ning, D., Li, B., 2020. Numerical simulation and experimental analysis of wave interaction with a porous plate. Ocean Eng. 218, 108106.
Qiao, D., Mackay, E., Yan, J., Feng, C., Li, B., Feichtner, A., Ning, D., Johanning, L., 2021. Numerical simulation with a macroscopic CFD method and experimental analysis of wave interaction with fixed porous cylinder structures. Mar. Struct. 80, 103096.
Rezanejad, K., Gadelho, J., Soares, C.G., 2019. Hydrodynamic analysis of an oscillating water column wave energy converter in the stepped bottom condition using CFD. Renew. Energy 135, 1241–1259.
Romolo, A., Arena, F., 2013. Three-dimensional non-linear standing wave groups: Formal derivation and experimental verification. Int. J. Non-Linear Mech. 57, 220–239.
Romolo, A., Arena, F., Laface, V., 2014. A generalized approach to the mechanics of three-dimensional nonlinear ocean waves. Probab. Eng. Mech. 35, 96–107.
Romolo, A., Timpano, B., Laface, V., Fiamma, V., Arena, F., 2024. Small-scale field experiment on wave forces on a U-OWC breakwater. Coast. Eng. 189, 104476.
Rusche, H., 2003. Computational Fluid Dynamics of Dispersed Two-Phase Flows at High Phase Fractions (Ph.D. thesis). Imperial College London (University of London).
Shao, Z., Gao, H., Liang, B., Lee, D., 2022. Potential, trend and economic assessments of global wave power. Renew. Energy 195, 1087–1102.
Simonetti, I., Cappietti, L., 2021. Hydraulic performance of oscillating water column structures as anti-reflection devices to reduce harbour agitation. Coast. Eng. 165, 103837.
Simonetti, I., Cappietti, L., Elsafti, H., Oumeraci, H., 2018. Evaluation of air compressibility effects on the performance of fixed OWC wave energy converters using CFD modelling. Renew. Energy 119, 741–753.
Sollitt, C.K., Cross, R.H., 1972. Wave transmission through permeable breakwaters. In: Coastal Engineering. pp. 1827–1846.
Tiron, R., Mallon, F., Dias, F., Reynaud, E.G., 2015. The challenging life of wave energy devices at sea: A few points to consider. Renew. Sustain. Energy Rev. 43, 1263–1272.
Tsai, C.P., Ko, C.H., Chen, Y.C., 2018. Investigation on performance of a modified breakwater-integrated OWC wave energy converter. Sustainability 10 (3), 643.
Van Doormaal, J.P., Raithby, G.D., 1984. Enhancements of the SIMPLE method for predicting incompressible fluid flows. Numer. Heat Transfer 7 (2), 147–163.
Viviano, A., Musumeci, R.E., Vicinanza, D., Foti, E., 2019. Pressures induced by regular waves on a large scale OWC. Coast. Eng. 152, 103528.
Wang, R.Q., Ning, D.Z., Zhang, C.W., Zou, Q.P., Liu, Z., 2018. Nonlinear and viscous effects on the hydrodynamic performance of a fixed OWC wave energy converter. Coast. Eng. 131, 42–50.
Wang, R.Q., Ning, D.Z., Zou, Q.P., 2020. Wave loads on a land-based dual-chamber oscillating water column wave energy device. Coast. Eng. 160, 103744.
Wang, S., Xu, T.J., Dong, G.H., Wang, T.Y., 2023b. Numerical simulation of damping effect of ballast water system on motion response of immersed tunnel element. Ocean Eng. 281, 114795.
Wang, S., Xu, T.J., Dong, G.H., Wang, T.Y., Chen, L.Y., 2022b. Numerical simulation of anti-sloshing performance in a 2D rectangular tank with random porous layer. Ocean Eng. 265, 112660.
Wang, B., Xu, T.J., Jiang, Z.Q., Wang, S., Dong, G.H., Wang, T.Y., 2022a. Numerical simulation of sloshing flow in a 2D rectangular tank with porous baffles. Ocean Eng. 256, 111384.
Wang, S., Xu, T.J., Shen, K.M., Wang, B., Dong, G.H., Wang, T.Y., 2023c. Numerical simulation of the interaction between nonlinear sloshing flow and side-mounted perforated baffles. Phys. Fluids 35 (8), 083607.
Wang, C., Xu, H., Zhang, Y., Chen, W., 2023a. Hydrodynamic investigation on a three-unit oscillating water column array system deployed under different coastal scenarios. Coast. Eng. 104345.
Zeng, X., Shao, Y., Feng, X., Xu, K., Jin, R., Li, H., 2024. Nonlinear hydrodynamics of floating offshore wind turbines: A review. Renew. Sustain. Energy Rev. 191, 114092.
Zhang, Y., Zhao, X., Geng, J., Tao, L., 2021. A novel concept for reducing wave reflection from OWC structures with application of harbor agitation mitigation/coastal protection: Theoretical investigations. Ocean Eng. 242, 110075.
Zheng, S., Meylan, M., Greaves, D., Iglesias, G., 2020. Water-wave interaction with submerged porous elastic disks. Phys. Fluids 32 (4).
Zhou, Y., Ning, D., Liang, D., Qiao, D., 2022. Nonlinear wave loads on an offshore oscillating-water-column wave energy converter array. Appl. Ocean Res. 118, 103003.